



Adsorption and degradation of sulfadiazine over nanoscale zero-valent iron encapsulated in three-dimensional graphene network through oxygen-driven heterogeneous Fenton-like reactions

Yujia Yang^a, Lejin Xu^{a,b,*}, Wuyang Li^a, Weijie Fan^a, Shuang Song^c, Jun Yang^{a,b}

^a Department of Nuclear Engineering and Technology, School of Energy and Power Engineering, Huazhong University of Science and Technology, Wuhan 430074, PR China

^b State Key Laboratory of Coal Combustion, School of Energy and Power Engineering, Huazhong University of Science and Technology, Wuhan 430074, PR China

^c College of Environment, Zhejiang University of Technology, Hangzhou 310032, PR China

ARTICLE INFO

Keywords:

Nanoscale zero-valent iron
Three-dimensional graphene
Adsorption
Oxidation
Sulfadiazine

ABSTRACT

Fe-based heterogeneous Fenton-like catalysts has shown tremendous potential for wastewater treatment, but the investigation of adsorption, reduction and oxidation mechanism remains challenging. In this study, nanoscale zero-valent iron encapsulated in three-dimensional graphene network (3D-GN@nZVI) was synthesized and characterized as a heterogeneous Fenton-like catalyst via the activation of dissolved oxygen (DO) for adsorption and degradation of sulfadiazine (SDZ). 3D-GN@nZVI had the synergistic effect of catalytic reactivity for sulfadiazine removal, which was evaluated in view of the effects of operational factors. The role of adsorption, reduction and oxidation was determined; in 3D-GN@nZVI/DO system, sulfadiazine was removed mainly by the attack of hydroxyl radicals ($\cdot\text{OH}$). The possible degradation pathway of sulfadiazine was inferred by identifying reactive oxidizing species and degradation intermediates. According to the X-ray photoelectron spectroscopy (XPS) analysis, Fourier Transform infrared spectroscopy (FTIR) analysis and density functional theory (DFT) calculations, the distribution and transfer of electrons on the surface of 3D-GN@nZVI were illustrated, and the adsorption and oxidation mechanisms of sulfadiazine through DO-driven and micro-electrolysis-enhanced heterogeneous Fenton-like reaction were proposed. The comprehensive mechanism was elucidated to provide new insights to advance the DO-driven Fenton-like process and to inspire the development of nZVI and relevant composites.

1. Introduction

Nanoscale zero-valent iron (nZVI), as an environmentally benign material, is one of the most versatile engineered nanomaterials for efficient removal of heavy metals [1–3], organic dyes [4–6], pesticides and antibiotics [7–10] in environment remediation. Under anoxic conditions, nZVI can act as a reducing agent for removal of heavy metal ions and dehalogenation of chlorinated organic pollutants [6,11–13]. Under oxidation conditions, the application of nZVI for the degradation of various organic pollutants by activating peroxide oxidants, such as persulfate ($\text{S}_2\text{O}_8^{2-}$), peroxymonosulfate (HSO_5^-) and hydrogen peroxide (H_2O_2), has attracted much attention [14–16]. It is worthy to note that nZVI can also activate oxygen to generate H_2O_2 and induce a Fenton-like reaction for the oxidation of organic contaminations, which may be more economical for industrial-scale applications in water treatment [17,18]. Furthermore, microscopic and spectroscopic

studies have indicated that nZVI generally consists of zero-valent iron and an oxidized surface layer [19,20]. For the presence of these two constituents, the nZVI particles have the coordination properties and electron-donating capabilities, which may offer a unique combination for the adsorption and degradation of contaminations in water. Fu et al. [21] utilized nZVI modified by starch to remove tetracycline from solution with a high efficiency (99%), 30% of which was attributed to the adsorption and degradation, and 69% of which was due to flocculation. The superior properties of nZVI derive from the function of unique size and morphology of the nanoparticles. However, they are easy to agglomerate to form larger aggregates caused by van der Waals attraction and magnetic forces, rendering them inactivated and inapplicable for the targeted purposes [22–24].

To alleviate the agglomeration and to enhance the performance of nZVI, many researchers attempt to immobilize nZVI onto various matrix materials, including silica [25,26], carbon materials [22,27], resin

* Corresponding author at: Department of Nuclear Engineering and Technology, School of Energy and Power Engineering, Huazhong University of Science and Technology, Wuhan 430074, PR China.

E-mail address: xulejin@hust.edu.cn (L. Xu).

<https://doi.org/10.1016/j.apcatb.2019.118057>

Received 16 May 2019; Received in revised form 30 July 2019; Accepted 3 August 2019

Available online 10 August 2019

0926-3373/ © 2019 Elsevier B.V. All rights reserved.

[4,28], cellulose [29–31] and clay materials [32]. Among these carrier materials, graphene has attracted increasing attention due to its unique chemical and physical properties. Graphene is a two-dimensional single sheet consisting of numerous hexagonal carbon rings, which is inherent with many outstanding characteristics, such as large specific surface area, excellent optical transparency, strong chemical stability and high carrier mobility [33–35]. Graphene-based materials have been investigated and utilized as a promising support material to synthesize various novel composites for the adsorption and degradation of organic pollutants in aqueous solution. Wu et al. [36] prepared a superparamagnetic graphene-Fe₃O₄ nanocomposite by a facile one-pot solvothermal method for efficient adsorption of the organic dye pararosaniline from aqueous solution. Isari et al. [37] used Fe-doped TiO₂ anchored on reduced graphene oxide for photocatalytic degradation of rhodamine B and real textile wastewater. Moreover, Farooq et al. [38] synthesized graphene-oxide-supported nZVI composite as an efficient percarbonate activator for the degradation of 1,1,1-trichloroethane (TCA). Due to the strong π - π interaction between the graphene sheets, the graphene is easy to stack, thereby decreasing the specific surface area of the graphene and reducing the utilization of graphene. To solve this problem, many studies have constructed three-dimensional graphene (3D-GN), which retains the inherent characteristics of graphene with a unique porous structure and enhanced properties [39,40]. In our previous work, 3D-GN was utilized as a support for zero-valent copper nanoparticles to assemble 3D-GN@Cu⁰ composite for metronidazole degradation [41]. Although 3D-GN@Cu⁰ exhibited satisfactory catalytic performance, the secondary pollution from Cu²⁺ leaching and the separation problem inhibited the application of 3D-GN@Cu⁰. Therefore, nZVI is more competitive due to its environmental safety and magnetic property. In addition to the promising catalytic potential, Fe species are capable of removing pollutants by flocculation. These attractive properties and mechanisms of Fe-related composites are worthy of further investigation and exploration in details for potential application.

The adsorption and Fenton-like oxidation of organic pollutants are affected by the physicochemical properties of the catalyst surface, solution pH, reaction temperature and so on [42–46]. Guo and Zhang [43] have synthesized a bifunctional Fe-montmorillonite composite for photo-Fenton discoloration of rhodamine B. The high discoloration efficiency of rhodamine B could be ascribed to the synergetic effects of the enhanced adsorption power of the composite and the hydroxyl radicals initiated through the heterogeneous photo-Fenton process. Liu et al. [44] have investigated the adsorption and catalytic wet hydrogen peroxide oxidation of methylene blue (MB) by Fe₃O₄ nanoparticles-decorated reduced graphene oxide magnetic nanocomposites (Fe₃O₄/rGO NCs). Under acidic conditions, with the positively charged surface of the Fe₃O₄/rGO NCs, the adsorption of MB decreased, and the degradation efficiency of MB was mainly attributed to the generation of radicals by the reaction of Fe₃O₄ with H₂O₂. Under alkaline conditions, the negatively charged surface of the Fe₃O₄/rGO NCs favored the adsorption of cationic MB molecule, and the removal of MB was ascribed to the adsorption and the attack of oxidative species, such as hydroxyl radicals (\cdot OH) and high-valent iron species ($=\text{Fe}^{\text{IV}}=\text{O}$). Because the mechanisms of adsorption/precipitation and Fenton-like oxidation by various catalysts are complicated, the active sites on the surface of catalysts and the electron transfer process require detailed investigation. Whether the oxidative reactions carried out mainly on the surface of the catalysts or in the aqueous solution also need to be further studied.

The synthetic antibiotic under study (sulfadiazine) is widely used in veterinary and human medicine, and the presence of the antibiotic in aquatic environment can cause antibiotic resistance, becoming the potential health hazards to ecosystem [47]. The objective of this study was to effectively remove sulfadiazine (SDZ) in water by a combined adsorption and oxygen-driven heterogeneous Fenton process using the nanoscale zero-valent iron encapsulated in three-dimensional graphene

network (3D-GN@nZVI). 3D-GN@nZVI was synthesized by a self-assembled liquid-phase reduction process, and the physical and chemical characterization of 3D-GN@nZVI was carried out. The application of this composite in oxygen-driven heterogeneous Fenton reaction was investigated in view of the effects of reaction conditions (i.e., pH, sulfadiazine concentration, 3D-GN@nZVI dose, temperature, co-existing cations, gases and radical scavengers) on the removal of sulfadiazine. The possible mechanisms associated with adsorption and oxidation of sulfadiazine are addressed through the execution of the experiments, instrumental analysis and density functional theory (DFT) calculations.

2. Materials and methods

2.1. Chemicals and reagents

Sulfadiazine (C₁₀H₁₀N₄O₂S; 98%) was purchased from Aladdin Chemistry Co., Ltd. (Shanghai, China). Graphite powder was supplied by Nanjing XFANO Materials Tech. Co., Ltd. Potassium borohydride (KBH₄), ferrous sulfate heptahydrate (FeSO₄·7H₂O), hydrogen peroxide (H₂O₂, 30 wt%), sulfuric acid (H₂SO₄), sodium nitrate (NaNO₃), calcium nitrate (Ca(NO₃)₂), KI and *n*-butanol were provided by Sinopharm Chemical Reagent Co., Ltd. All chemicals used in this work were of analytical reagent grade without further purification. Argon (Ar) gas was supplied by Huarwen Industrial Co., Ltd. (Wuhan, China), and deionized water was employed.

2.2. Preparation and characterization of catalysts

A simple self-assembly process of the liquid-phase reduction was used to synthesize the nZVI particles anchored on 3D crumpled macroporous graphene. According to Hummer's methods [48], graphene oxide (GO) was prepared by the oxidation of graphite powder and dehydrated. After dispersing 0.8 g of GO in 100 mL of ultrapure water for 2 h by ultrasonic dispersion, the obtained GO suspension was stirred with KBH₄ (3.24 g) at room temperature for 24 h under Ar atmosphere. Then, 50 mL 50 mM FeSO₄·7H₂O aqueous solution was added dropwise (1 mL/min) to the mixture of GO and KBH₄ with constant stirring for 1 h under Ar protection at ambient temperature, and Fe²⁺ was reduced by KBH₄ to form Fe⁰ nanoparticles. After the composite was deposited, it was rinsed with ultrapure water, and finally dried in a vacuum freeze-dryer.

The morphology of the 3D-GN@nZVI composite was identified by a ZEISS Sigma 300 field emission scanning electron microscopy (FSEM) with an InLens detector. After degassing the 3D-GN@nZVI at 80° for 5 h, the N₂ adsorption-desorption method was used to measure the Brunauer–Emmett–Teller (BET) specific surface areas and pore size distributions using the nonlocal density functional theory (NL-DFT) by an ASAP 2020 BET sorptometer. Raman spectra were determined by a Bruker FRA 106/S spectrometer with a 532-nm laser source. The crystal pattern was characterized by an X-ray diffractometer (X' Pert Powder) using Cu K α radiation (λ = 1.5418 Å, 40 kV, 40 mA) at a scanning rate of 5°/min in the range of 5° to 90°. X-ray photoelectron spectrometry analyses (XPS, AXIS-ULTRA DLD-600W) were performed, and the results were analyzed and fitted using the XPS-peak 4.1 software. The solid samples of 3D-GN@nZVI before and after reaction were mixed with potassium bromide and pressed to form tablets, and then analyzed by Fourier transform infrared spectrometer (FTIR, VERTEX 70, Bruker, Germany).

2.3. Electrochemical tests

The electrochemical performance of the oxygen reduction reaction (ORR) activity of the prepared catalysts was evaluated at ambient temperature by cyclic voltammetry (CV) and linear sweep voltammetry (LSV) with a rotating disk electrode (RDE, Pine AFMSRCE rotator), which was measured at a CHI 660b electrochemical workstation. Ag/

AgCl electrode, Pt wire and glassy carbon disk (0.07 cm² area) modified with the catalyst layer were used as the reference, counter, and working electrode, respectively. 0.1 M KOH solution was served as the electrolyte. The catalysts ink was prepared by dispersing 5 mg catalysts in a mixture of 450 μ L ethanol and 50 μ L Nafion solution with sonication for 1 h. Then, 7 μ L homogenous catalyst suspension was pipetted onto the surface of the glassy carbon electrode and dried in the air.

CV measurements in ORR experiments were conducted in Ar or O₂ saturated electrolytes at a scan rate of 50 mV/s. LSV tests were performed in the O₂ saturated electrolyte with the electrode rotating at various speeds (400–2000 rpm) at a scan rate of 10 mV/s. The slope of the Koutecky–Levich plot (K–L plot) is used to analyze the number of electrons (*n*) transferred during the ORR on the basis of the K–L equations:

$$J^{-1} = J_K^{-1} + (B\omega^{1/2})^{-1} \quad (1)$$

$$B = 0.2nFC_0D_0^{2/3}\nu^{-1/6} \quad (2)$$

where *J*, *J_K* and ω are total current density, dynamic current density and electrode rotation speed, respectively. *B* is the Levich slope of J^{-1} vs. $\omega^{1/2}$. *n*, *F*, *C₀*, *D₀* and ν are the electrons exchanged per oxygen molecule, Faraday constant (96,485 C/mol), the bulk concentration of O₂ (1.21 $\times 10^{-6}$ mol/cm³), the diffusion coefficient of O₂ (1.9 $\times 10^{-5}$ cm²/s) and the kinematic viscosity of the electrolyte (0.01 cm²/s), respectively.

2.4. Experimental procedure

The experiments were carried out in unsealed serum bottles (20 mL) in the dark. Unless otherwise specified, the experiments were triggered with 0.5 g/L of 3D-GN@nZVI catalyst and 10 mL of sulfadiazine solution (10 mg/L), which was continuously shaken at 150 rpm under aerobic conditions. In air-saturated solution, the dissolved oxygen was about 7.5 mg/L; for the argon-purging experiment, the dissolved oxygen was decreased to 0–0.1 mg/L. The addition of H₂SO₄ (0.1 M) or NaOH (0.1 M) was performed to adjust the initial pH of the sulfadiazine solution. In reaction process, samples were withdrawn at set intervals, and filtered immediately through 0.22- μ m membranes for analyses. Each experiment was carried out in duplicate, and average values are presented.

To reveal the effect of pH on nZVI dissolution and DO consumption, the experiment was performed in a 200 mL glass flask with a stirring rate of 150 rpm at 298 K. Briefly, the reaction was triggered by the addition of 0.5 g/L 3D-GN@nZVI and 100 mL SDZ solution (10 mg/L) at pH 1.0 and 3.0. To investigate the dissolution of nZVI, 1 mL solution was taken at different time intervals to measure the concentration of Fe ions by an atomic absorption spectrophotometer (AAS, WFX-220B, Rayleigh, China). Moreover, the variation of DO in the solution was monitored by a dissolved oxygen meter (JPB-607A, Shanghai Precision and Scientific Instrument Co., Ltd., China).

2.5. Sample analysis

The concentration of sulfadiazine was quantified by a high-performance liquid chromatography (HPLC, Waters 1525, USA) equipped with a C18 reversed-phase column (5 μ m, 4.6 \times 150 mm) and a diode array detector. The mobile phase was 0.02 mol/L sodium acetate solution and acetonitrile (80:20, v/v) with a flow rate of 1.0 mL/min. The detection wavelength and temperature were set at 278 nm and 35 $^{\circ}$ C, respectively. The solution pH was measured by a pH meter (PHS-3E, Shanghai INESA Scientific Instrument Co., Ltd.). A Bruker EPR A300 electron paramagnetic resonance spectrometer (EPR, Germany) was used to detect superoxide anion radicals ($\text{O}_2^{\cdot-}$) and hydroxyl radicals (OH^{\cdot}) trapped by 5,5-dimethyl-1-pyrroline-N-oxide (DMPO). After 10 mg of 3D-GN@nZVI was ultrasonically dispersed in 10 mL of deionized water for 5 min with the adjustment of pH, 200 μ L of the

suspension was taken out and immediately mixed with 50 μ L of 0.1 M DMPO to form a DMPO-radical adduct, which was determined by the EPR spectrometer. The degradation intermediates of sulfadiazine were identified by an Agilent 1100 liquid chromatography and an electrospray ionization tandem mass spectrometry (LC/MS, USA) equipped with a Waters BEH-C18 column (5 μ m, 4.6 \times 150 mm).

2.6. DFT calculations

All DFT calculations were performed by Gaussian 16 software, and the models were created using GaussView 5.0. The hybrid Becke-3-Lee Yang Parr (B3LYP) density functional method with the 6–31 G(d,p) basis set was used for all elements except for Fe [49]. For models involving Fe, the SDD pseudopotential and the corresponding basis sets were applied [50]. Analytic frequencies were calculated after all structural optimizations to ensure that all structures were the local minima on the potential surface. Meanwhile, D3 dispersion corrections [51] were applied, and the SMD solvation model [52] was chosen to simulate the effect of water.

The geometries of sulfadiazine and its intermediates were optimized using the B3LYP density functional method with the 6–31 G (d) basis set [51]. Frequency analyses were calculated at the same level in order to ensure that all structures are local minima (no imaginary frequencies) as well as to obtain the infrared spectral information.

3. Results and discussion

3.1. Characterization of 3D-GN@nZVI

The microstructure of the synthesized 3D-GN@nZVI was observed by the low- and high-magnification SEM images as shown in Fig. 1a and b. As seen in Fig. 1a, the multi-layer graphene is assembled hierarchically into a three-dimensional morphology, forming a complex porous structure on the surface of 3D-GN@nZVI. By further amplification (Fig. 1b), it can be clearly observed that many spherical particles with an average particle size of 120–200 nm are embedded in the folded and porous structure of graphene matrix. After the self-assembly reduction process, since the oxygen-containing groups remain on the graphene sheets, the hydrogen on the oxygen-containing group is positively charged, and graphene substrates are negatively charged [53,54]. Fe²⁺ could be captured by the negatively charged graphene substrates, which facilitates the distribution of nZVI particles in the 3D-GN matrix.

To further evaluate the surface properties of 3D-GN@nZVI, the specific surface area and the NL-DFT pore size distribution were measured as shown in Fig. 1c and d, respectively. The nitrogen adsorption-desorption isotherms of 3D-GN@nZVI can be characterized as type IV with H3 hysteresis loop, suggesting the presence of the mesoporous structure [24,55]. Based on the Brunauer-Emmett-Teller (BET) analysis, the specific surface area of 3D-GN@nZVI was measured to be 20.1 m²/g with a pore volume of 0.050 cm³/g. The pore size distribution curve with double peaks (Fig. 1d) shows that the pore size of 3D-GN@nZVI was mainly concentrated at 3.2 and 4.5 nm, which may be caused by the slit of flexible graphene sheets and some voids of the wrapped Fe⁰ particles.

Raman spectra of 3D-GN and 3D-GN@nZVI are shown in Fig. 1e, and two well-known sharp peaks representing the G and D bands of graphene appear at 1339 cm^{−1} and 1575 cm^{−1}. In addition, the 2D overtone band and D + G combination band were observed at 2675 cm^{−1} and 2924 cm^{−1}, respectively, which were introduced by disordered and staggered graphene sheets [56,57]. For the 3D-GN matrix and the 3D-GN@nZVI composite, the intensity ratio of the D and G bands (*I_D*/*I_G*) is 1.25, indicating that the introduction of nZVI has little effect on the structure of the 3D-GN matrix.

X-ray diffraction patterns of the synthesized nZVI and 3D-GN@nZVI are shown in Fig. 1f. The main characteristic diffraction peak at 44.6 $^{\circ}$

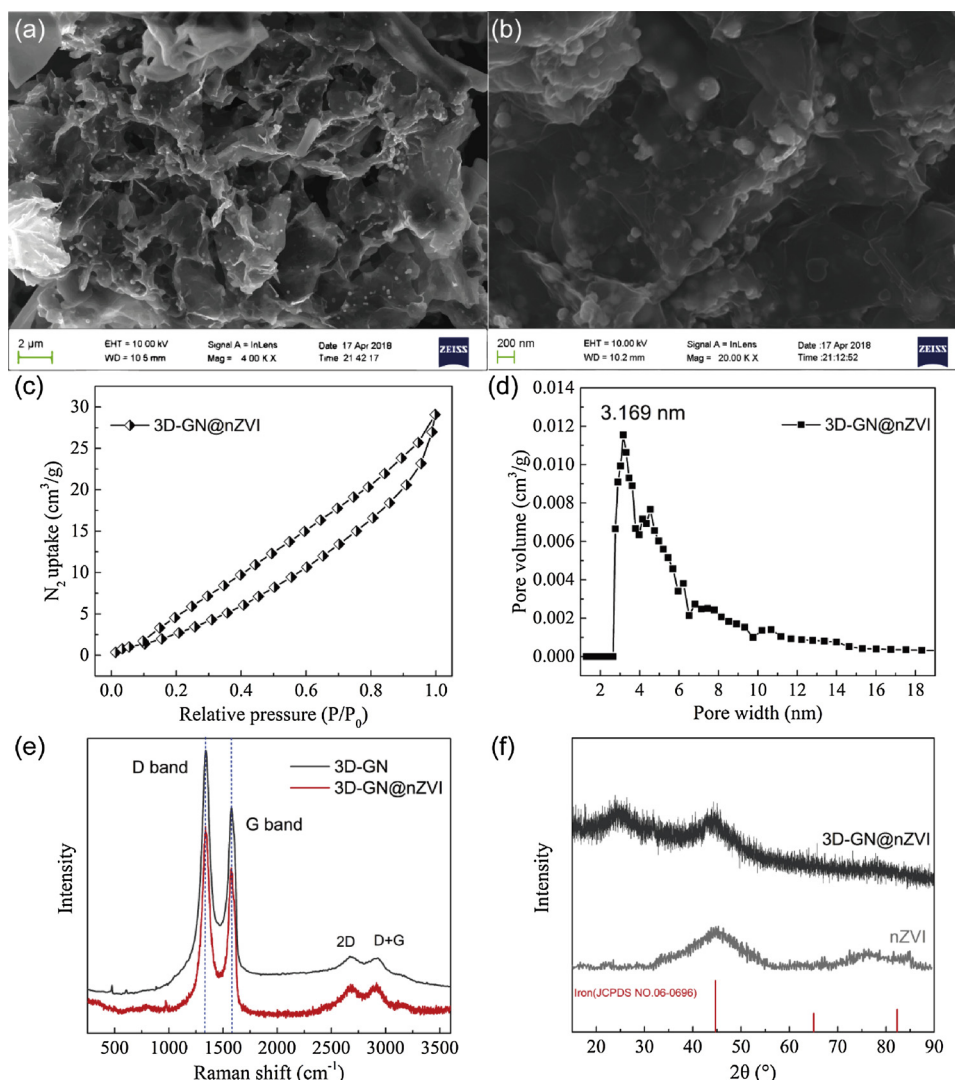


Fig. 1. (a) Low-magnification and (b) high-magnification SEM images of 3D-GN@nZVI. (c) Nitrogen adsorption-desorption isotherms and (d) NL-DFT pore size distribution curve of 3D-GN@nZVI. (e) Raman spectra of 3D-GN and 3D-GN@nZVI. (f) XRD patterns of nZVI and 3D-GN@nZVI.

was observed in the XRD patterns of two materials, which is assigned to the (110) plane of α -Fe (body-centered cubic structure, space group Im-3 m (229)) corresponding to the standard card of JCPDS 06-0696. From XRD reflection of 3D-GN@nZVI, a weak broad diffraction peak at diffraction angles (2θ) of about 25° is attributed to the (002) plane of graphene crystalline [58].

3.2. DFT analysis of the reactive center on the catalyst

To further investigate the catalytic reactivity and reactive center of materials, the electrostatic potential distribution and HOMO/LUMO spatial analysis of materials were investigated by using the DFT calculation. According to the Koopmans' theorem, the highest occupied molecular orbital (HOMO) is related to the ionization potential, and the lowest unoccupied molecular orbital (LUMO) is related to the electron affinity, thus the HOMO-LUMO gap is generally considered as an indicator of kinetic stability and chemical reactivity to some extent [59]. Fig. 2a displays an optimized graphene fragment with several oxygen-containing functional groups (such as -OH), representing the GN matrix produced by incomplete reduction of graphene oxide [60]. The Mulliken charges labeling on the atoms show that the boundary C and H atoms bonded with O atoms are positive, and O atoms are electro-negative; the electric charge of these C atoms is much higher than the

charge of other C atoms on the GN rings. The simplified model of 3D-GN@nZVI was formed by introducing a Fe atom on the simplified graphene substrate, and its optimized geometric structure is shown in Fig. 2b. After the introduction of the Fe atom, the electronic distribution of the hexatomic ring (π -electron) adjacent to the Fe atom was significantly decreased. It is observed that the atomic charge values of C₂ and C₅ atoms on the hexatomic ring of 3D-GN@nZVI were decreased from 0.003 to -0.020 and -0.021, respectively, and the atomic charge value of C₃ and C₆ was decreased from -0.016 to -0.049. The Fe atom exhibits a relatively high positive atomic charge value of 0.337, inferring that the highly reactive Fe⁰ tends to transfer electrons to the GN. Moreover, the boundary C atoms bonded with O atoms have positive charge values, and O atoms have negative values, suggesting that there are electron-deficient areas around Fe atom and the boundary C atoms bonded with O atoms, and there are electron-rich areas around the other C atoms (such as C₂, C₃, C₅ and C₆) and O atoms. These electro-positive/negative regions are potential surface reactive sites for the oxidation/reduction reaction, which can provide the reactive center for the catalytic reaction [59,61]. Therefore, numerous micro-electrolytic cells will be formed between nZVI particles and GN matrix, which could accelerate the oxidation of nZVI and activation of dissolved oxygen.

The HOMO and LUMO spatial distributions for the GN and 3D-GN@nZVI are presented in Fig. 3. The red and green regions represent the

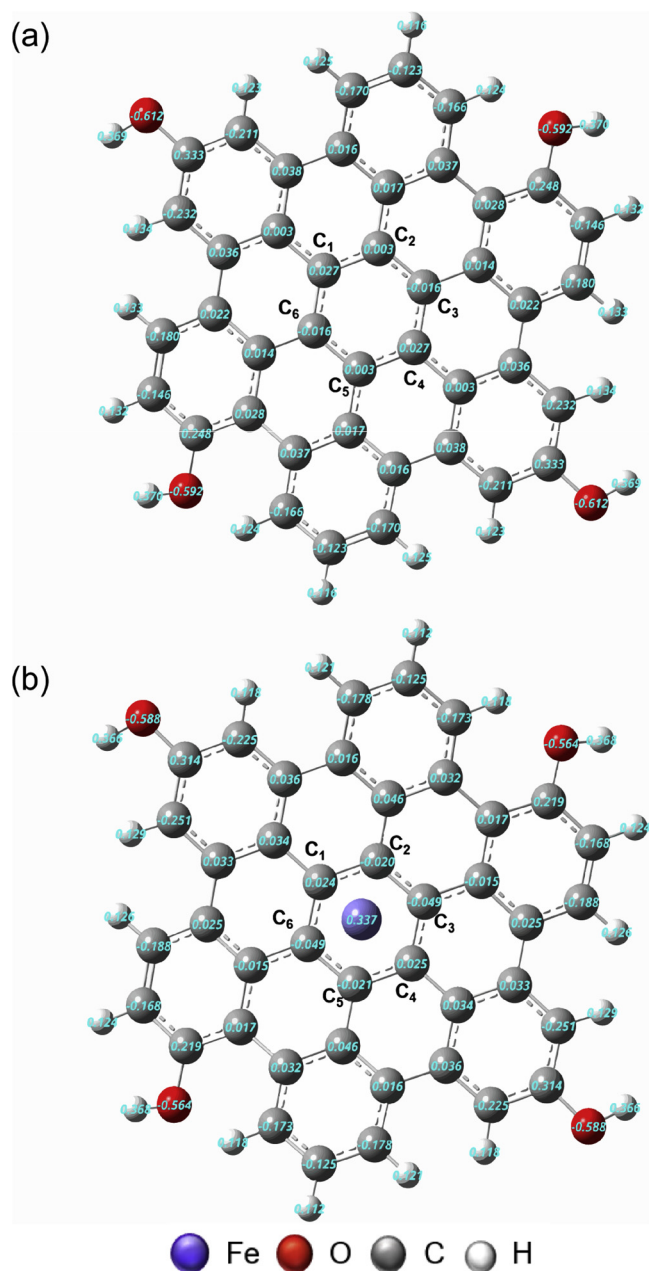


Fig. 2. Charge distribution of the GN matrix (a) and 3D-GN@nZVI (b) with the Mulliken charge values of the atoms.

positive and negative values of the phase of the molecular orbital wave function, respectively. For the GN model, both HOMO and LUMO spatial distributions are delocalized, and its HOMO-LUMO gap was calculated to be 0.12 (Table 1). For the 3D-GN@nZVI, the HOMO spatial distribution was located on the Fe atom, and the LUMO was mainly distributed on the GN, which means that Fe^0 was supposed to be the electron donor, and the GN matrix preferred to accept the electron. Compared to GN, the lower HOMO-LUMO gap of 3D-GN@nZVI (0.083) indicated that 3D-GN@nZVI has higher chemical and catalytic reactivity due to the synergistic effect of nZVI and GN.

3.3. Influence of operational factors on sulfadiazine removal

The catalytic property of 3D-GN@nZVI in the oxygen-driven heterogeneous Fenton-like reaction was evaluated in view of the effect of some main variables, including various catalysts, pH, initial concentration of sulfadiazine, 3D-GN@nZVI dose, temperature, and co-

existing cations, as shown in Fig. 4. The catalytic activity of nZVI, GN, 3D-GN@nZVI and the mixture of nZVI and GN was compared for the removal of sulfadiazine in the presence of dissolved oxygen (DO) with 10 mg/L sulfadiazine and 0.5 g/L catalyst at pH 3.0 and T 298 K. As depicted in Fig. 4a, after 120 min of reaction about 18% and 23% removal of sulfadiazine were observed in air-saturated solutions with 0.5 g/L nZVI and 0.5 g/L GN, respectively, which was mainly expected to surface adsorption. However, the mixture of nZVI and GN with the mass ratio of 1:4 effectively enhanced the removal efficiency to 67% within 120 min, ascribed to the surface adsorption and catalytic oxidation. The removal efficiency of sulfadiazine was further improved to 81% using 3D-GN@nZVI as the catalyst, which revealed the synergistic effect of sulfadiazine removal between the two components resulted from the promoted electrons transfer and the enhanced chemical reactivity at the reactive sites. Therefore, the 3D-GN@nZVI exhibited a promising catalytic activity for ORR. This result was also confirmed by the DFT analysis which revealed the formation of the reactive centers on the 3D-GN@nZVI. It is worth mentioning that the 3D-GN@nZVI composite exhibits a high efficiency for sulfadiazine removal without adding H_2O_2 or aeration, indicating that it is a promising method in the treatment of low-concentration polluted wastewater.

Since the pH value has an important influence on the catalytic performance, the production and the oxidizing ability of oxidizing substances [62–64], the effect of pH on the removal efficiency of sulfadiazine was examined as seen in Fig. 4b. When pH increased from 1.0 to 3.0, the sulfadiazine removal within 120 min was enhanced from 49% to 81%. Under extremely acidic conditions ($\text{pH} < 3$), nZVI would be corroded very quickly resulting in the low utilization of Fe^0 , and hydrogen ions could scavenge $\cdot\text{OH}$ [10,65]. Based on the leaching experiment of Fe ions (Fig. 5a), nZVI dissolved more severely under extremely acidic condition (pH 1.0) compared to acidic condition (pH 3.0), which could inhibit the activation of DO. The change of DO during the reaction was also investigated at pH 1.0 and 3.0 as seen in Fig. 5b. The consumption of DO followed pseudo-first-order kinetics, and the reaction rate at pH 3.0 was much faster than that at pH 1.0, which indicates that at pH 3.0, 3D-GN@nZVI was more favorable to stimulate DO generating $\cdot\text{OH}$. Further increasing the pH from 3.0 to 7.0 led to a significant decrease in the removal efficiency of sulfadiazine (from 81% to only 12% within 120 min), which was because under neutral and alkaline conditions, iron oxide and iron hydroxide would form a passivation film on the surface of the 3D-GN@nZVI, inhibiting iron corrosion and contact with contaminants [10]. The lower removal efficiency at higher pH values can also be resulted from the lower oxidation potential of hydroxyl radicals and the decomposition of H_2O_2 generated spontaneously in situ [62,63]. Thus, the highest removal efficiency of sulfadiazine by 3D-GN@nZVI was observed at pH 3.0 in this study, and this condition was both favor the utilization of Fe^0 and electron transfer, which is consistent with the removal of antibiotics (e.g., metronidazole and chloramphenicol) by nZVI reported in previous studies [10,66].

Initial concentration of sulfadiazine and the dosage of 3D-GN@nZVI are also important factors that affect the reaction. As shown in Fig. 4c, the removal efficiency of sulfadiazine was decreased at higher sulfadiazine concentrations, because the active sites on 3D-GN@nZVI became relatively limited, and dissolved oxygen was continuously consumed [10]. When initial sulfadiazine concentration was 2 mg/L, approximately 94% of sulfadiazine was removed within 5 min, indicating that 3D-GN@nZVI could remove low-concentrations of sulfadiazine quickly and efficiently. Fig. 4d presents the effect of 3D-GN@nZVI dosage on the removal of sulfadiazine in air-saturated solutions with 10 mg/L sulfadiazine at pH 3.0 and T 298 K. When the 3D-GN@nZVI dosage was increased from 0.2 g/L to 0.7 g/L, the removal of sulfadiazine after 120 min moderately increased from 50% to 88%, which indicates that the active site on 3D-GN@nZVI plays an important role in the removal of sulfadiazine. A larger dose of 3D-GN@nZVI increases the number of active sites on the catalyst surface, and enhances

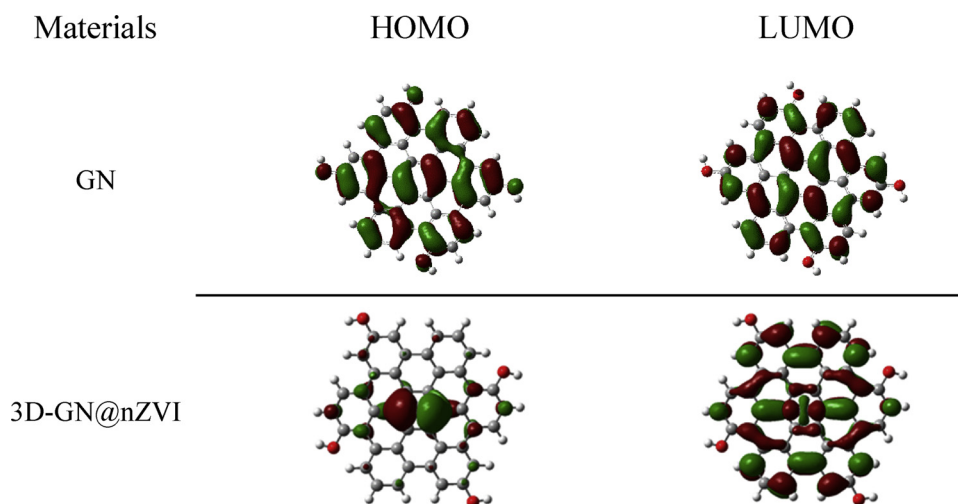


Fig. 3. HOMO and LUMO spatial distribution of GN matrix and 3D-GN@nZVI.

Table 1

HOMO, LUMO and HOMO-LUMO energy gap for GN matrix and 3D-GN@nZVI (unit: eV).

Spin	GN	3D-GN@nZVI
HOMO	−0.184	−0.131
LUMO	−0.064	−0.048
HOMO-LUMO gap	0.12	0.083

the release of Fe^{2+} into water, accelerating the reactions with dissolved oxygen and H_2O_2 , finally generating more oxidative radicals [67].

The removal of sulfadiazine within a reaction temperature range of 293–313 K has been examined for 3D-GN@nZVI composite (Fig. 4e). It is evident that temperature had little effect on the removal of sulfadiazine. NaNO_3 and $\text{Ca}(\text{NO}_3)_2$ were employed to reveal the effect of common cations (Na^+ and Ca^{2+}) and ionic strength (0.01 M and 0.1 M) on SDZ elimination by 3D-GN@nZVI, respectively. As shown in Fig. 4f, the coexisting of $\text{Na}^+/\text{Ca}^{2+}$ posed a negligible effect on the removal of SDZ despite the cation concentration is as high as 0.1 M.

3.4. Role of adsorption, reduction and oxidation

As a highly efficient heterogeneous Fenton catalyst [68], 0.5 g/L 3D-GN@nZVI was used to catalyze 3 mM H_2O_2 at different pHs to remove sulfadiazine, which was compared to the removal process without the addition of H_2O_2 . As shown in Fig. 6a, under acidic or neutral conditions, the removal efficiency was improved to some extent by the addition of H_2O_2 , due to the generation of more $\cdot\text{OH}$. At pH values of 3.0 and 4.0, the removal efficiency of sulfadiazine by the catalytic reaction of 3D-GN@nZVI with H_2O_2 was 98% and 92%, respectively, which was nearly 17% and 25% higher than that without H_2O_2 . With the increase of pH, the removal rate of sulfadiazine was significantly decreased with or without the addition of H_2O_2 . At pH 7.0, in 3D-GN@nZVI/DO systems with and without H_2O_2 , removal efficiencies were reduced to 27% and 12%, respectively. For the 3D-GN@nZVI/ H_2O_2 system, the removal of sulfadiazine was mainly ascribed to the oxidation of hydroxyl radicals produced by the Fenton reaction of 3D-GN@nZVI with H_2O_2 , which was highly affected by the pH value. Comparatively, the removal of sulfadiazine in the 3D-GN@nZVI/DO system exhibited a similar process, implying that 3D-GN@nZVI could activate dissolved oxygen in situ to form H_2O_2 further generating $\cdot\text{OH}$. Whether H_2O_2 was added in the solution or not, the concentration of H_2O_2 was too low to be detected. Several previous studies using various heterogeneous Fenton-like catalysts (such as Zn-Fe-CNTs and sulfide modified nZVI composite) have investigated and detected the generation of H_2O_2 by the reaction

between catalysts and O_2 in aqueous solution [63,69].

To investigate the role of adsorption, reduction and oxidation in the removal of sulfadiazine by 3D-GN@nZVI/DO system, experiments were carried out with Ar purging and with the addition of radical scavengers, as shown in Fig. 6b and c, respectively. When purging with Ar before the reaction (Fig. 6b), about 44% and 25% sulfadiazine were removed after 120 min at pH 3.0 and pH 5.0, respectively, primarily attributed to the surface adsorption and reduction of 3D-GN@nZVI. The removal efficiencies were much lower than that under aerobic conditions, indicating that dissolved oxygen played an important role in the removal of sulfadiazine. Herein, *n*-butanol is used to quench the $\cdot\text{OH}$ both in the bulk solution ($\cdot\text{OH}_{\text{free}}$) and on the surface of catalyst ($\cdot\text{OH}_{\text{ads}}$), and KI is used to eliminate $\cdot\text{OH}_{\text{ads}}$ and positive holes (h^+) on the catalyst surface [70,71]. As seen in Fig. 6c, the removal of sulfadiazine was strongly inhibited with the addition of excess *n*-butanol (50 mM), which suggested that the removal of sulfadiazine was mainly due to the action of hydroxyl radicals, including $\cdot\text{OH}_{\text{free}}$ and $\cdot\text{OH}_{\text{ads}}$. In the presence of *n*-butanol, about 11% and 6% sulfadiazine were removed after 120 min at pH 3.0 and pH 5.0, respectively, which were ascribed to the surface adsorption. At pH 3.0, the removal efficiency of sulfadiazine decreased significantly from 81% to 22% with excess KI (10 mM), which provided the evidence for the generation of $\cdot\text{OH}_{\text{ads}}$ on the surface of 3D-GN@nZVI and the primary role of $\cdot\text{OH}_{\text{ads}}$ and h^+ in the removal of sulfadiazine. However, at pH 5.0, excess KI caused a slight reduction of the sulfadiazine removal efficiency from 50% to 38%. Combined with the effect of *n*-butanol at pH 5.0, both $\cdot\text{OH}_{\text{free}}$ and $\cdot\text{OH}_{\text{ads}}$ played an important role in the removal of sulfadiazine. It could be concluded that the dissolved oxygen was essential for the generation of oxidative species (especially at pH 3.0) in the 3D-GN@nZVI/DO system without the extra addition of H_2O_2 . The production of $\cdot\text{O}_2^-$ and $\cdot\text{OH}$ in the 3D-GN@nZVI/DO system at pH 3.0 and pH 5.0 was further proved by the EPR spectra (Fig. 7). The 6-fold characteristic peak of $\text{DMPO}\cdot\text{O}_2^-$ adducts and the 4-fold characteristic peak of $\text{DMPO}\cdot\text{OH}$ adducts with an intensity ratio of 1:2:2:1 were observed, indicating the formation of $\cdot\text{HO}_2/\cdot\text{O}_2^-$ and $\cdot\text{OH}$ radicals in the 3D-GN@nZVI/DO system at pH 3.0 and pH 5.0. The intensity of these peaks at pH 3.0 was higher than that at pH 5.0, suggesting that more oxidative radicals were formed at pH 3.0, which was consistent with the above results obtained by the removal efficiencies of sulfadiazine and the effect of radical scavengers at pH 3.0 and pH 5.0.

Thus, at pH 3.0, after 120 min of reaction, about 11% sulfadiazine was removed attributed to the surface adsorption; 44% sulfadiazine was removed by 3D-GN@nZVI/Ar system primarily ascribed to the surface adsorption and reduction; 81% removal of sulfadiazine was obtained in 3D-GN@nZVI/DO system mainly by the oxidation of $\cdot\text{OH}_{\text{ads}}$; 98%

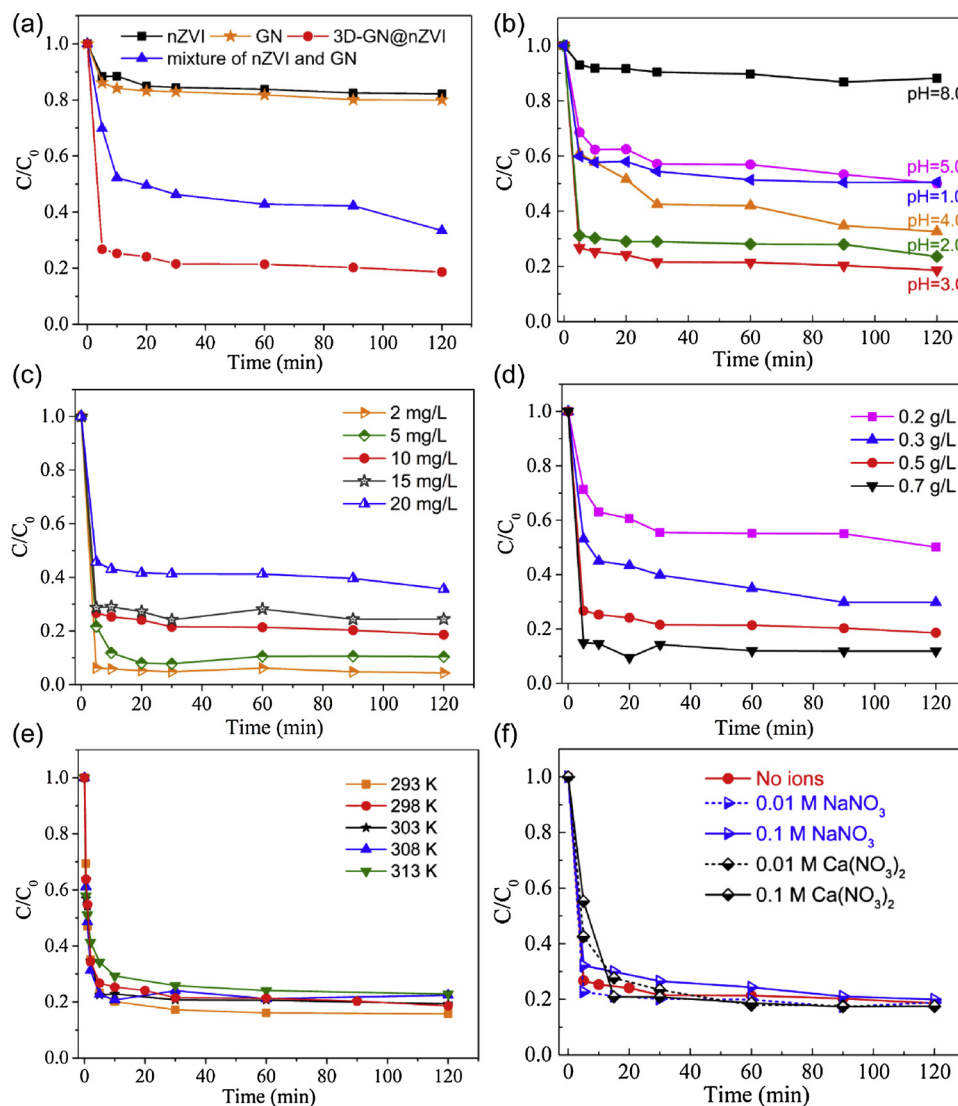


Fig. 4. Effect of operating parameters on sulfadiazine removal by oxygen-driven heterogeneous Fenton-like system: (a) various catalysts; (b) pH; (c) initial sulfadiazine concentration; (d) 3D-GN@nZVI addition; (e) temperature; (f) co-existing cations. Except for the investigated parameter, other parameters fixed on pH 3.0, initial sulfadiazine concentration 10 mg/L, 3D-GN@nZVI dose 0.5 g/L and temperature 298 K.

sulfadiazine was removed by 3D-GN@nZVI/ H_2O_2 system because of the generation of more $\cdot\text{OH}$. At pH 5.0, about 6%, 25%, 50% and 60% removal of sulfadiazine were observed in the systems of 3D-GN@nZVI/*n*-butanol, 3D-GN@nZVI/Ar, 3D-GN@nZVI/DO and 3D-GN@nZVI/ H_2O_2 , which were caused by adsorption, adsorption and reduction, the attack of $\cdot\text{OH}_{\text{free}}$ and $\cdot\text{OH}_{\text{ads}}$, and the oxidation of $\cdot\text{OH}$, respectively.

3.5. Catalytic performance towards ORR

To further reveal the catalytic properties of as-prepared materials, ORR measurements were performed. The cyclic voltammograms (CVs) of 3D-GN, nZVI and 3D-GN@nZVI are shown in Fig. 8. For 3D-GN, no peak was observed in the Ar-saturated electrolyte, and a significant

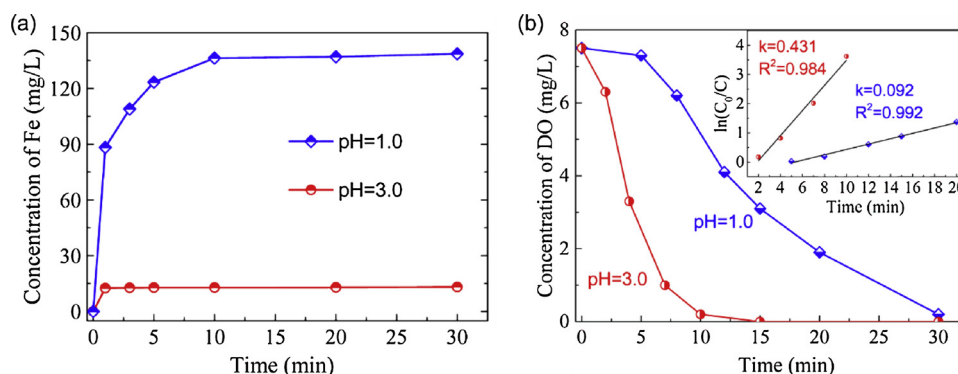


Fig. 5. (a) The leaching of Fe ions; (b) the variation of DO concentration and the kinetics of DO consumption (inset) at pH 1.0 and 3.0.

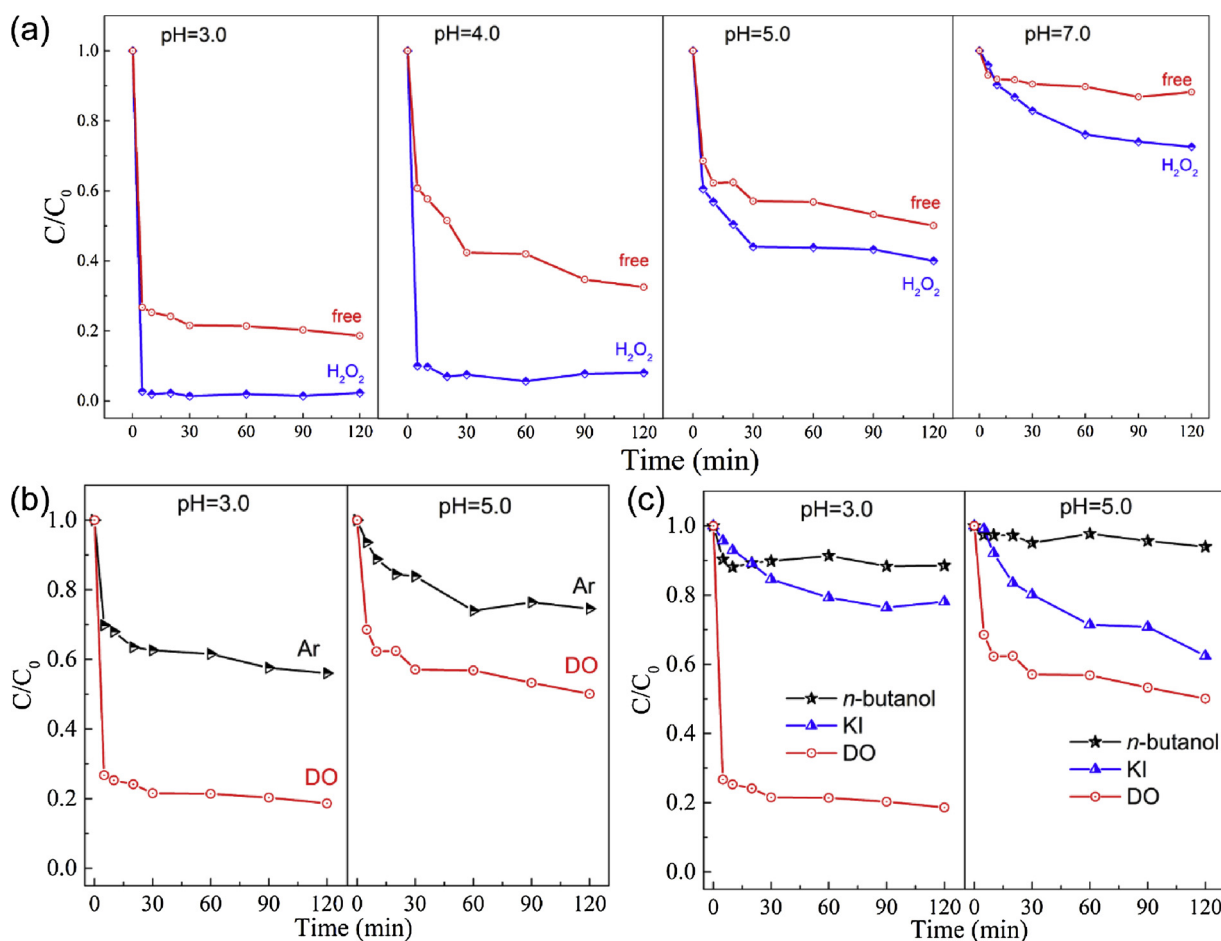


Fig. 6. (a) Removal efficiencies of sulfadiazine by 3D-GN@nZVI with and without H_2O_2 under different initial pH conditions; (b) removal efficiencies of sulfadiazine in the presence of dissolved oxygen (DO) and argon gas (Ar) at pH 3.0 and pH 5.0; (c) effect of radical scavengers on sulfadiazine removal at pH 3.0 and pH 5.0. Reaction conditions: initial sulfadiazine concentration 10 mg/L, 3D-GN@nZVI dose 0.5 g/L and temperature 298 K.

cathodic peak at 0.52 V was obtained in the O_2 -saturated electrolyte, which is ascribed to the oxygen reduction. The pure nZVI presented a quasi-rectangular voltammogram with no reduction peak in the Ar-saturated electrolyte; two weak reduction peaks were observed at 0.37 V and 0.55 V, which were related to the redox reaction of $2e^-$ and the redox reaction of $4e^-$, respectively [72–74]. For 3D-GN@nZVI, the oxygen reduction peak also appeared at 0.75 V, which shifted to the more positive region compared to the CVs of 3D-GN and nZVI, indicating that 3D-GN@nZVI exhibited better catalytic activity.

The catalytic performance was further confirmed by LSVs and the results are shown in Fig. 9. The electron-transfer number (n) of 0.45 V to 0.5 V was calculated by the K–L plot as seen in the inset of Fig. 9. For

3D-GN (Fig. 9a), n was approximately 2.0, implying a two-electron oxygen reduction process. The n obtained from nZVI towards ORR was 3.0 (Fig. 9b), which is due to the simultaneous processes of two-electron and four-electron transfer. In Fig. 9c, 3D-GN@nZVI exhibited a four-electron transfer process, which provided an evidence for the strong electron interaction between 3D-GN and nZVI.

3.6. Degradation pathway of sulfadiazine

To investigate the degradation pathway of sulfadiazine, the components of the liquid samples after the degradation reaction were identified by LC/MC in the positive ion mode. The mass spectrometry

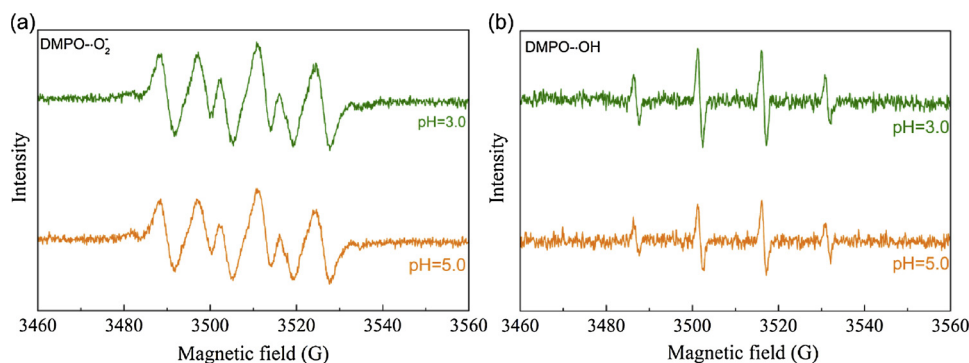


Fig. 7. EPR spectra of DMPO· O_2^- (a) and DMPO·OH (b) in the 3D-GN@nZVI/DO system at pH 3.0 and 5.0 with T 298 K.

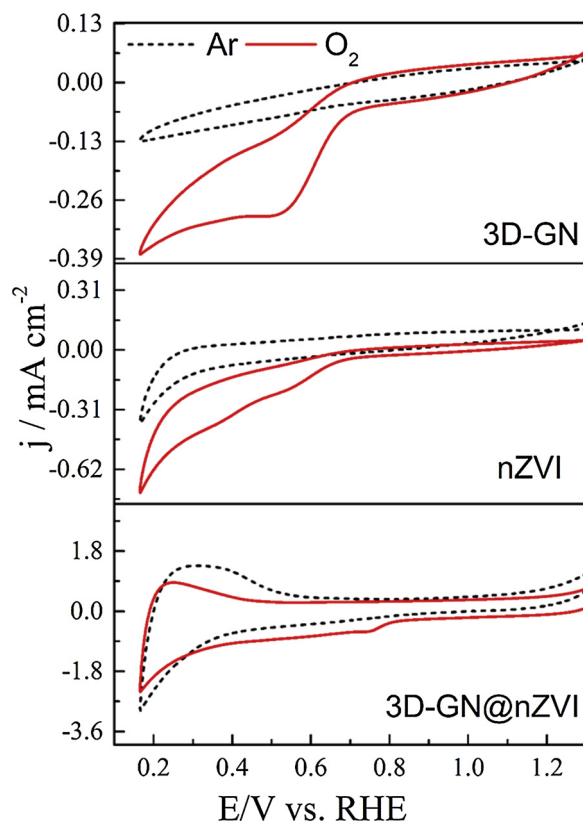


Fig. 8. Cyclic voltammograms of 3D-GN, nZVI and 3D-GN@nZVI.

data at different retention times are shown in Fig. 10, and the intermediates produced during the degradation process with initial sulfadiazine concentration of 10 mg/L and 3D-GN@nZVI dosage of 0.5 g/L at pH 3.0 and T 298 K are listed in Table 2, including retention time, mass to charge ratio and molecular structure. N-hydroxy-4-(2-(4-(N-(pyrimidin-2-yl) sulfamoyl) phenyl) hydrazineyl) benzene sulfonamide (P_1 , $m/z = 432$), 4-(2-phenylhydrazineyl)-N-(pyrimidin-2-yl) benzene sulfonamide (P_2 , $m/z = 340$), 4-amino-N-(pyrimidin-2-yl) benzene sulfonamide (P_3 , $m/z = 267$), 4-amino-N-carbamimidoylbenzenesulfonamide (P_4 , $m/z = 213$), 4-aminobenzenesulfonic acid (P_5 , $m/z = 174$) and 2-aminopyrimidine-4,6-diol (P_6 , $m/z = 127$) were identified. According to the medium lethal dose (LD_{50}) values, these intermediates are less toxic than sulfadiazine.

Considering the key role of $\cdot OH_{ads}$ in the removal of sulfadiazine at pH 3.0 discussed in the above section and taking into account the intermediates identified in Table 2, a possible reaction pathway for the oxidation of sulfadiazine by 3D-GN@nZVI/DO system at optimal pH 3.0 was proposed in Fig. 11. As reported by other previous studies [75,76], the N_1-H , S_8-N_{11} , $N_{13}-C_{14}$ and $C_{16}-N_{17}$ bonds on sulfadiazine as reactive sites were easily broken by attack of hydroxyl radicals. During the reaction, an electron tended to transfer from the N_1 site (α site) of sulfadiazine molecule to $\cdot OH$, and the N_1-H bond was cleaved to form a sulfadiazine radical, which was adsorbed on the surface of 3D-GN@nZVI. These active sulfadiazine radicals coupled with each other to form dimers [77,78]. Then the dimer of sulfadiazine radicals was attacked by $\cdot OH$ to yield intermediates P_1 and P_2 . The S_8-N_{11} bond (β site) on sulfadiazine was also cleaved by $\cdot OH$ to generate 4-aminobenzenesulfonic acid (P_5) and 2-aminopyrimidine-4,6-diol (P_6). In addition, the imidazole ring of sulfadiazine was attacked by $\cdot OH$ to form 4-amino-N-(pyrimidin-2-yl) benzene sulfonamide (P_3), which was further opened resulting in the formation of 4-amino-N-carbamimidoylbenzenesulfonamide (P_4). These intermediates could be further oxidized to smaller molecular organic acids (such as formic acid and acetic acid) and inorganic ions (such as NO_3^- , CO_2 and H_2O).

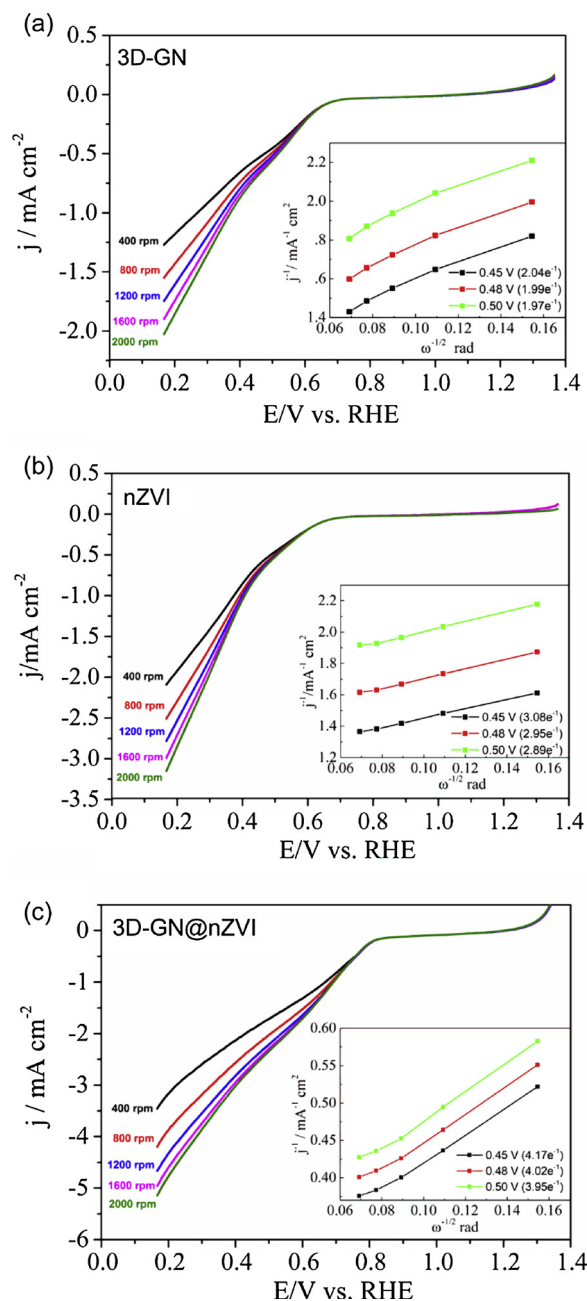


Fig. 9. LSVs and the corresponding K-L plots of (a) 3D-GN, (b) nZVI and (c) 3D-GN@nZVI at the potential range of 0.45 to 0.5 V (inset).

3.7. Adsorption and reaction mechanism

To further study the adsorption and reaction mechanism of sulfadiazine by 3D-GN@nZVI/DO system, surface structure information of 3D-GN@nZVI before and after reaction at pH 3.0 was analyzed by XPS spectra (Fig. 12), and the binding energy (BE) peaks of Fe 2p (Fig. 12a), N 1s (Fig. 12b), O 1s (Fig. 12c) and C 1s (Fig. 12d) were calibrated with C 1s BE at 284.6 eV. As shown in Fig. 12a, six characteristic peaks can be assigned to Fe(0) state (Fe $2p_{3/2}$: 706.9 eV), satellite peak of Fe 2p (Fe $2p_{1/2}$: 718.0 eV), Fe(II) state (Fe $2p_{1/2}$: 709.7 eV) and Fe(III) state (Fe $2p_{3/2}$: 710.8 eV; Fe $2p_{3/2}$: 713.0 eV; Fe $2p_{1/2}$: 724.6 eV), respectively [71,79,80]. The presence of Fe(II) and Fe(III) peaks indicated that a thin layer of iron oxide/hydroxide was wrapped outside the metallic iron (Fe^0) core, and the formation of the overlayer was inevitable during the preparation and frozen-dry process of 3D-GN@nZVI [79,81]. After 120 min of reaction, the Fe 2p photoelectron peaks (Fig. 12a)

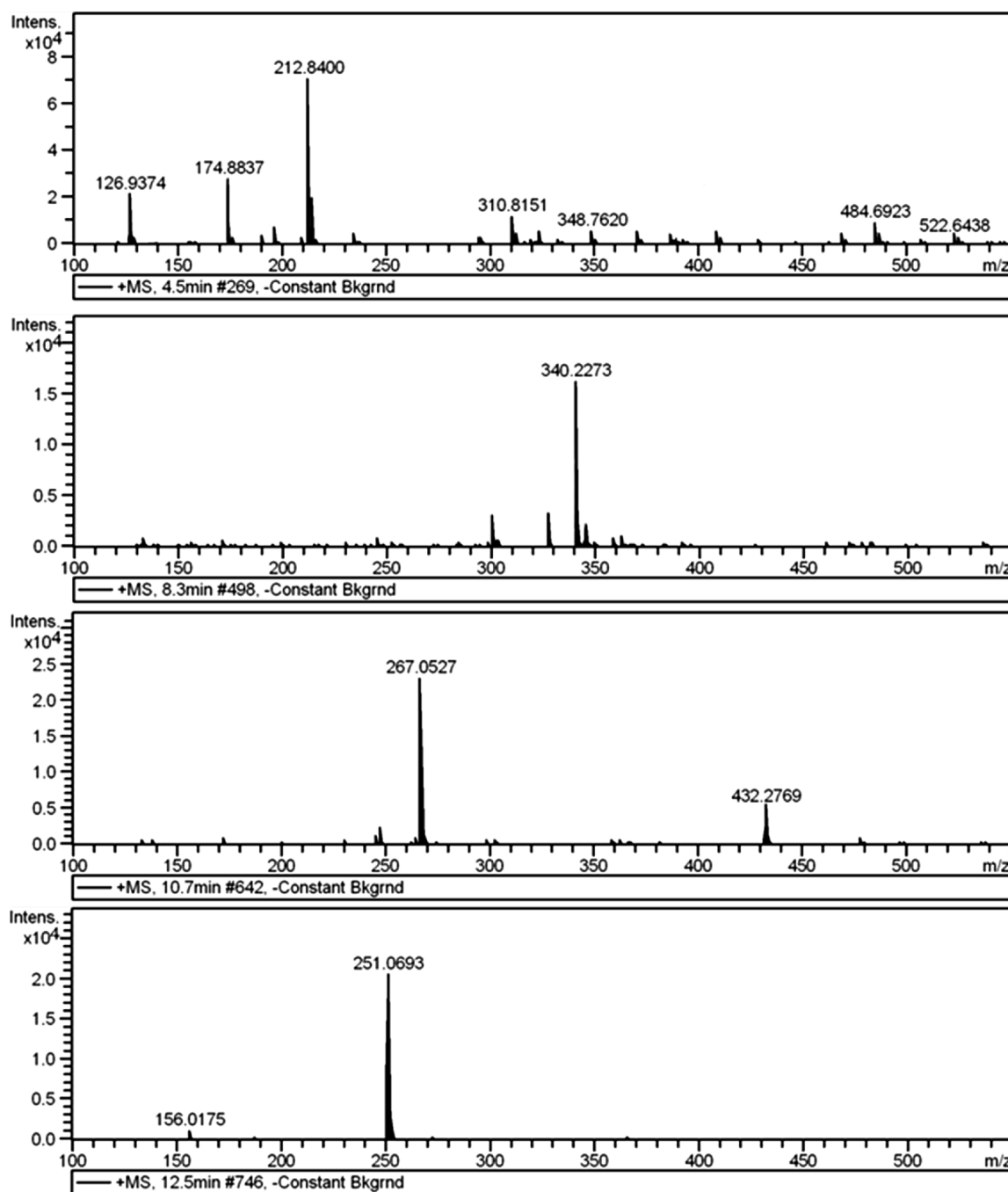


Fig. 10. The degradation intermediates of sulfadiazine detected by LC/MS with initial sulfadiazine concentration of 10 mg/L and 3D-GN@nZVI dosage of 0.5 g/L at pH 3.0 and T 298 K.

show that Fe(0) peak at 706.9 eV and the Fe(II) peak at 709.7 eV vanished, suggesting that on the catalyst surface the nZVI was oxidized. Moreover, the satellite peak at 718.0 eV shifted to 719.0 eV, and the peaks attributed to Fe(III) (Fe $2p_{3/2}$: 710.8; Fe $2p_{3/2}$: 724.6 eV) shifted to 711.5 eV and 725.6 eV, respectively, which may be due to the strong chemical bond between Fe (III) and SDZ [73].

In the N 1s scan spectra (Fig. 12b), a significant peak at 400.2 eV appeared after 120 min reaction compared to fresh 3D-GN@nZVI, which is ascribed to non-protonated organic nitrogen species, such as amine, imine and amide [82]. It is confirmed that SDZ or some intermediates containing organic nitrogen species were adsorbed onto the surface of 3D-GN@nZVI during the reaction. For the high-resolution XPS spectra of O 1s (Fig. 12c), obvious changes were observed before and after the reaction. Before reaction, there is only one peak at

531.5 eV assigned to the $-OH$ group on the surface of 3D-GN@nZVI. For the sample used, the content of surface $-OH$ group decreased from 100% to 25.3%, and H_2O (533.1 eV) was also observed. Two new peaks at 530.5 eV and 532.1 eV appeared, occupying 11.1% and 32.4%, which were attributed to the bonds of Fe-O and O-S=O, respectively. It indicates that the removal of SDZ on 3D-GN@nZVI was mainly dependent on the synergistic effect of adsorption and degradation. In Fig. 12d, three peaks attributed to C-C/C=C (284.8 eV), C-O (286.2 eV) and O=C-O (288.7 eV) were detected both in fresh and used 3D-GN@nZVI, which were fitted with three components of GN matrix [83]. After reaction, the content of O=C-O decreased from 10.2% to 5.8%, suggesting that some competing species replaced $-COOH$ on the surface of GN.

In order to further confirm the adsorption of intermediates on the

Table 2

Main intermediates during sulfadiazine degradation in 3D-GN@nZVI/DO system.

Compound	Retention time (min)	Mass/charge ratio (m/z)	Molecular structure
Sulfadiazine	12.5	251	
P ₁	10.7	432	
P ₂	8.3	340	
P ₃	10.7	267	
P ₄	4.5	213	
P ₅	4.5	174	
P ₆	4.5	127	

3D-GN@nZVI, FTIR measurements of fresh and used 3D-GN@nZVI samples were conducted. As shown in Fig. 13a, the peak observed at $\sim 3400\text{ cm}^{-1}$ is caused by the stretching vibration of O–H due to the presence of moisture in the samples. The band appearing at 1621 cm^{-1} is attributed to the stretching vibration of the C=C skeleton in aromatic rings. For fresh 3D-GN@nZVI, the peaks at 1455, 1283 and 1028 cm^{-1} correspond to carboxyl O=C–OH, epoxy C–OH and alkoxy C–OH, which are derived from oxygen-containing groups on the 3D-GN substrate. After the reaction, the spectrum of the reacted 3D-GN@nZVI showed some new peaks compared to the fresh sample, which were

identical to the characteristic peaks of C–N and C=N bonds in sulfadiazine. To further infer possible intermediates adsorbed on 3D-GN@nZVI, the calculated FTIR spectra of sulfadiazine and degradation intermediates (P₁–P₆) identified in Table 2 were performed using DFT methods. The experimental FTIR spectra of sulfadiazine and used 3D-GN@nZVI and the DFT calculated spectra of sulfadiazine and its intermediates (mainly P₁ and P₂ fitted better) were compared in Figs. 13b and 13c. As seen in Fig. 13b, the difference between the experimental and simulated curves of sulfadiazine is minimal, which revealed that the calculated FTIR spectrum has a good agreement with the experimental curve. After comparing Fig. 13b and c, in the range of $700\text{--}1700\text{ cm}^{-1}$, the calculated spectra of P₁ and P₂ are similar to the curve of sulfadiazine, showing apparent vibrations of C–N bond (1460 cm^{-1}) and C=N bond (1357 cm^{-1}). Combined with the analysis of Fig. 11, it is indicated that P₁ and P₂ are the possible degradation intermediates adsorbed on the surface of 3D-GN@nZVI. Therefore, the removal of sulfadiazine by 3D-GN@nZVI/DO system includes both the adsorption of sulfadiazine and its intermediates on the catalyst surface and the oxidation degradation attacked by $\cdot\text{OH}$.

The adsorption of sulfadiazine, P₁ and P₂ on the surface of 3D-GN@nZVI was simulated by the DFT calculation as displayed in Fig. 14. The length between atom N of the imidazole ring on sulfadiazine and atom Fe of 3D-GN@nZVI is 1.93 \AA , and the lengths of atoms C of carbon ring on graphene and the atom Fe of 3D-GN@nZVI are $2.04\text{--}2.25\text{ \AA}$, showing that sulfadiazine is more easily adsorbed on Fe of 3D-GN@nZVI (Fig. 14a). When the intermediate P₁ was adsorbed on the surface of 3D-GN@nZVI as seen in Fig. 14b, the lengths between atoms C of carbon ring on graphene and the atom Fe of 3D-GN@nZVI become longer ($2.04\text{--}2.53\text{ \AA}$), and the benzene ring on P₁ is deformed by adsorption with the lengths of Fe–C₁' and Fe–C₂' of 1.97 and 2.03 \AA , respectively. Similar results are observed when P₂ was adsorbed on the surface of 3D-GN@nZVI as shown in Fig. 14c. Thus, the favored adsorption site for sulfadiazine, P₁ and P₂ is Fe on the surface of 3D-GN@

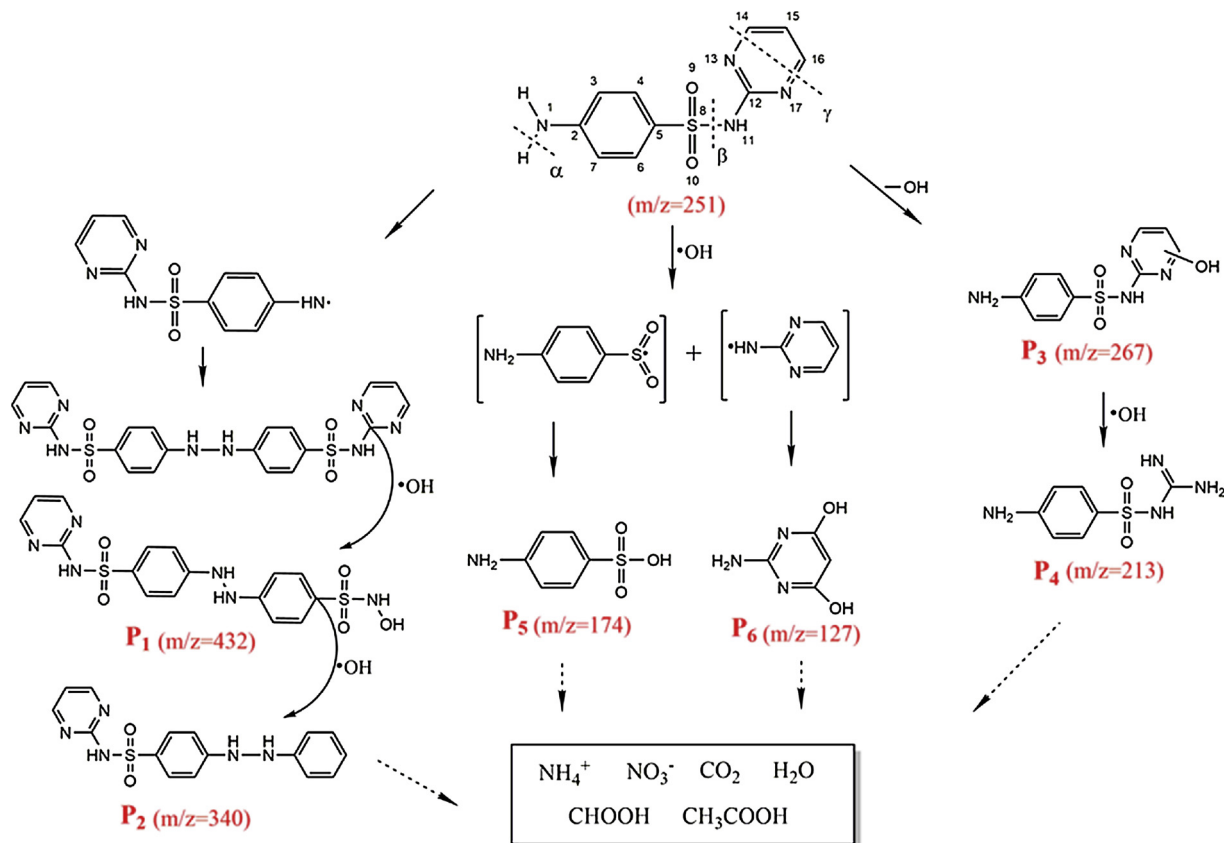


Fig. 11. Proposed reaction pathway for the oxidation of sulfadiazine at pH 3.0 by 3D-GN@nZVI/DO system.

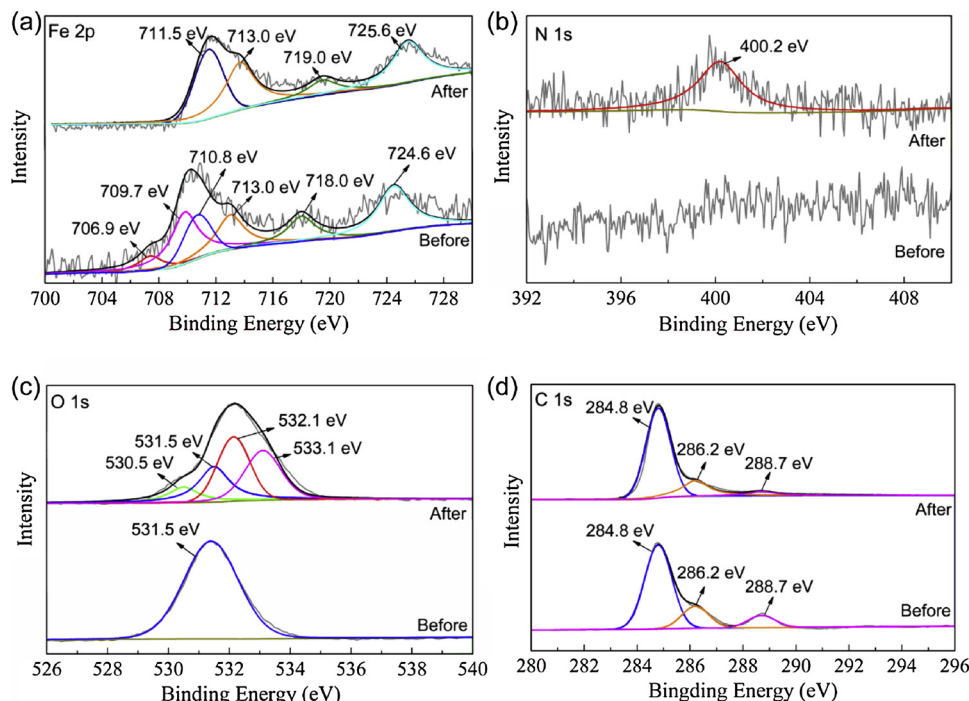


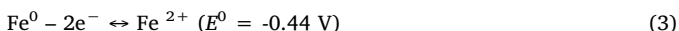
Fig. 12. High-resolution XPS spectra of Fe 2p (a), N 1s (b), O 1s (c), and C 1s (d) of 3D-GN@nZVI before and after reaction at pH 3.0 and T 298 K with initial sulfadiazine concentration of 10 mg/L and 3D-GN@nZVI dosage of 0.5 g/L.

nZVI.

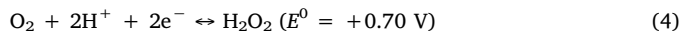
The electrostatic potential (ESP) of the optimized structure of 3D-GN@nZVI model was employed to map the electron density around 3D-GN@nZVI, which vividly reveals the tendency of electron transfer to facilitate the derivation of specific reaction mechanism. As presented in Fig. 15, the color code of the map indicates that the potential varies from negative to positive, corresponding to the color changing from red to blue. It is observed that the color around the Fe atom is light blue, implying that around Fe^0 on the 3D-GN@nZVI is the electron-deficient region, and the pale yellow of GN matrix represents the electron-rich region, as described in Section 3.2. Herein, the GN matrix acts as a good electrical conductor in combination with nZVI as an electron donor to form numerous microscopic galvanic-type corrosion cells for the degradation of sulfadiazine by 3D-GN@nZVI.

From the above findings, the adsorption and oxidation mechanism of sulfadiazine over 3D-GN@nZVI through oxygen-driven heterogeneous Fenton-like reactions was proposed as shown in Fig. 15. For the micro-electrolysis process, due to the lower standard potential of $\text{Fe}^{2+}/\text{Fe}^0$ (-0.44 V) [84], Fe^0 is liable to lose electrons as the anode (Eq. 3); the GN matrix as the cathode facilitates to transfer electrons to the dissolved oxygen to form H_2O_2 ($\text{O}_2/\text{H}_2\text{O}_2 = 0.70$ V) (Eq. 4). The Fe^{2+} species generated on the catalyst surface can react with dissolved oxygen through a series of one-electron transfer forming $\cdot\text{O}_2^-$ and transient H_2O_2 (Eqs. 5 and 6). In acidic conditions, the Fe^{2+} species can also catalyze the H_2O_2 generated in situ, further producing $\cdot\text{OH}$ radicals (Eq. 7); at pH > 5, a weaker and more selective oxidant such as ferryl ion (e.g., FeO^{2+}) is dominantly formed by reaction (8) [62]. Sulfadiazine and its intermediates are adsorbed onto the Fe sites of 3D-GN@nZVI and oxidized by these reactive oxygen species, mainly by $\cdot\text{OH}_{\text{ads}}$ at pH 3.0. The Fe^{3+} species are reduced to Fe^{2+} to continue the radical chain reactions (such as Eq. 9). Finally, oxyhydroxide and hydroxide are yielded through the reactions of Fe^{3+} with H_2O and OH^- (Eqs. 10 and 11), which coprecipitate with sulfadiazine and its intermediates on the surface of 3D-GN@nZVI (Eq. 12) [70].

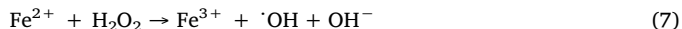
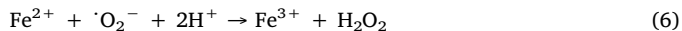
nZVI anode:



GN cathode:



Radicals chain reactions [85]:



Adsorption and deposition:



4. Conclusions

In this study, 3D-GN@nZVI was successfully synthesized as an efficient and environmental benign catalyst for sulfadiazine removal, which can in situ produce H_2O_2 further forming oxidative species via the activation of DO. The unique porous structure and physicochemical properties of 3D-GN@nZVI were characterized by the SEM, nitrogen adsorption/desorption isotherms, Raman spectroscopy and XRD patterns. To investigate the catalytic activity of 3D-GN@nZVI, reactive centers on the catalyst were analyzed, and the influence of operational factors on sulfadiazine removal was studied. Through the effects of Ar purging and radical scavengers, determination of reactive oxidizing species and degradation intermediates, the possible degradation pathway of sulfadiazine dominated by $\cdot\text{OH}_{\text{ads}}$ at pH 3.0 in 3D-GN@nZVI/DO system was proposed. Combined with the results of XPS analysis, FTIR spectra and DFT calculations, the anchored nZVI particles, as the adsorption sites and electron donors, were the adsorption

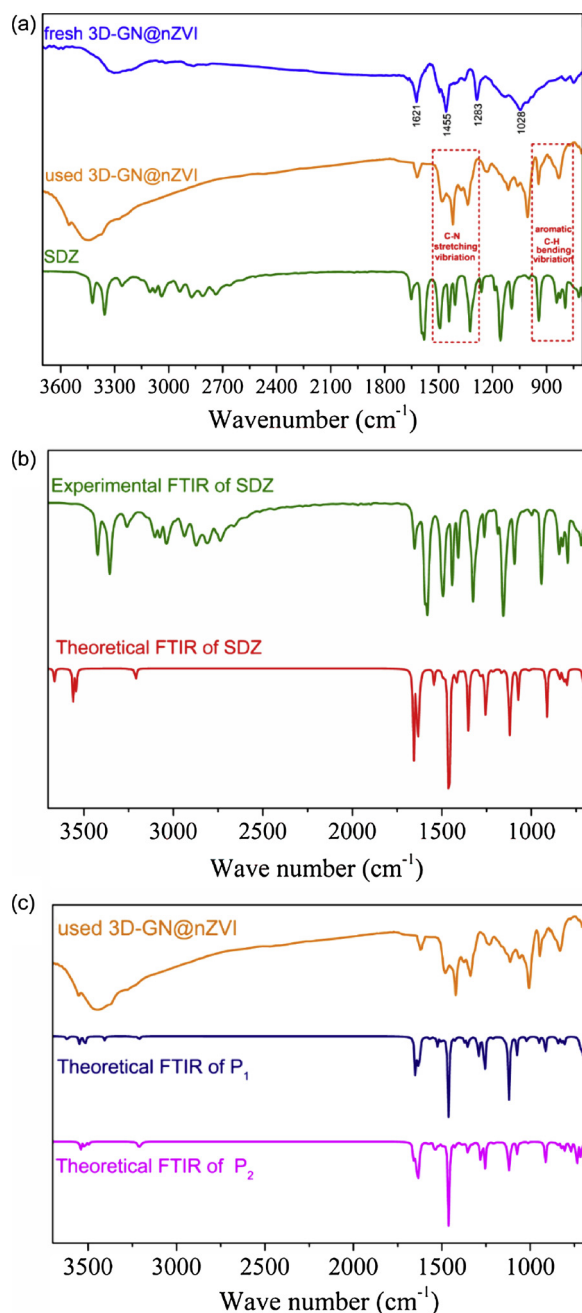


Fig. 13. (a) FTIR spectra of sulfadiazine, fresh and used 3D-GN@nZVI, (b) the experimental and calculated FTIR spectra of sulfadiazine, (c) the experimental FTIR spectra of reacted 3D-GN@nZVI and the calculated FTIR spectra of intermediates. Reaction conditions: pH 3.0, T 298 K, initial sulfadiazine concentration 10 mg/L and 3D-GN@nZVI dosage 0.5 g/L.

and reactive centers for sulfadiazine and its intermediates. Due to the excellent electronic conductivity of 3D-GN matrix, numerous micro-electrolytic cells formed surround the nZVI particles, which would facilitate to activate dissolved oxygen and trigger the Fenton-like reaction for the degradation of sulfadiazine. The mechanisms of adsorption and oxidation will provide a theoretical basis for the application of this system without purging O₂ or adding extra H₂O₂ in the treatment of low-concentration antibiotic wastewater.

The excellent catalytic properties of 3D-GN@nZVI via the activation of DO for adsorption and degradation of SDZ have been studied in detail. However, because the reduction of DO by electrons generated from the oxidation of Fe⁰ to Fe²⁺ is spontaneous, there are some

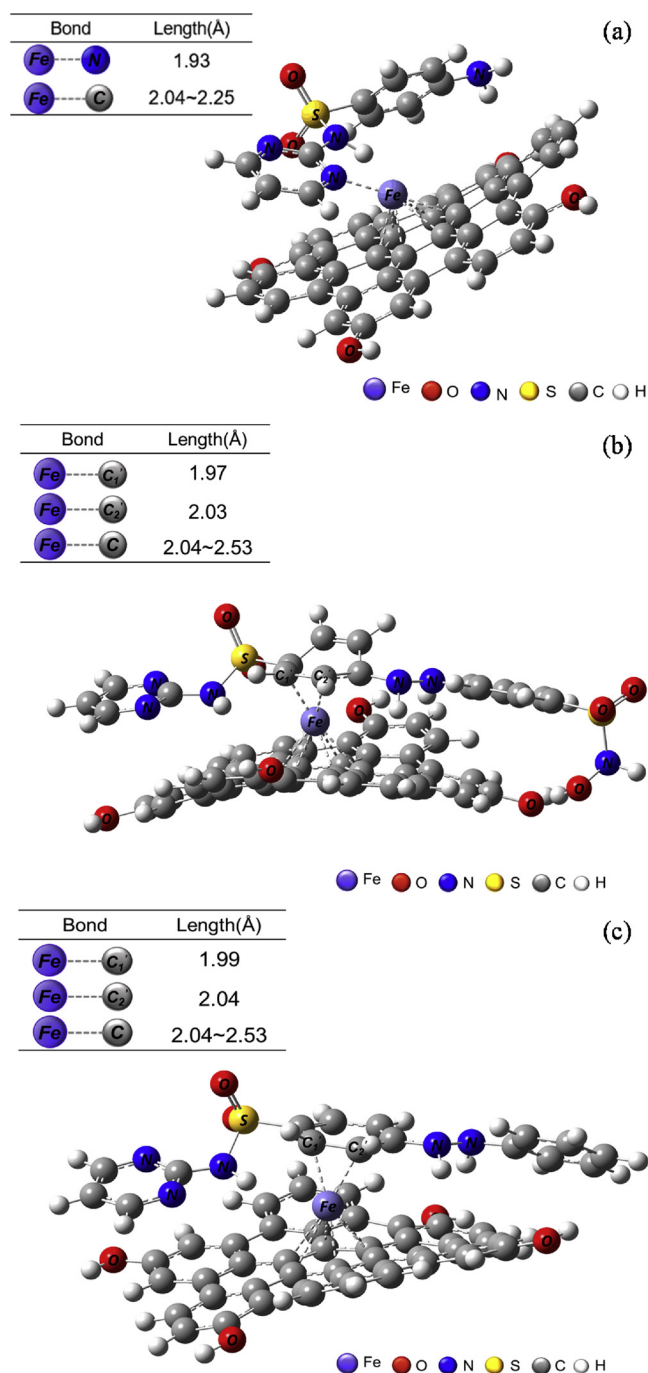


Fig. 14. The proposed adsorption mechanism of (a) sulfadiazine, (b) N-hydroxy-4-(2-(4-(N-(pyrimidin-2-yl) sulfamoyl) phenyl) hydrazineyl) benzene sulfonamide (P₁) and (c) 4-(2-phenylhydrazineyl)-N-(pyrimidin-2-yl) benzene-sulfonamide (P₂) on the surface of 3D-GN@nZVI.

deficiency in the durability and reuse of 3D-GN@nZVI. Future study is ongoing to improve the durability of catalyst by doping transition metals. How to reduce the dissolution of active components from the catalyst is also one of our future subjects.

Declaration of Competing Interest

The authors declare that they have no known competing financial interests or personal relationships that could have appeared to influence the work reported in this paper.

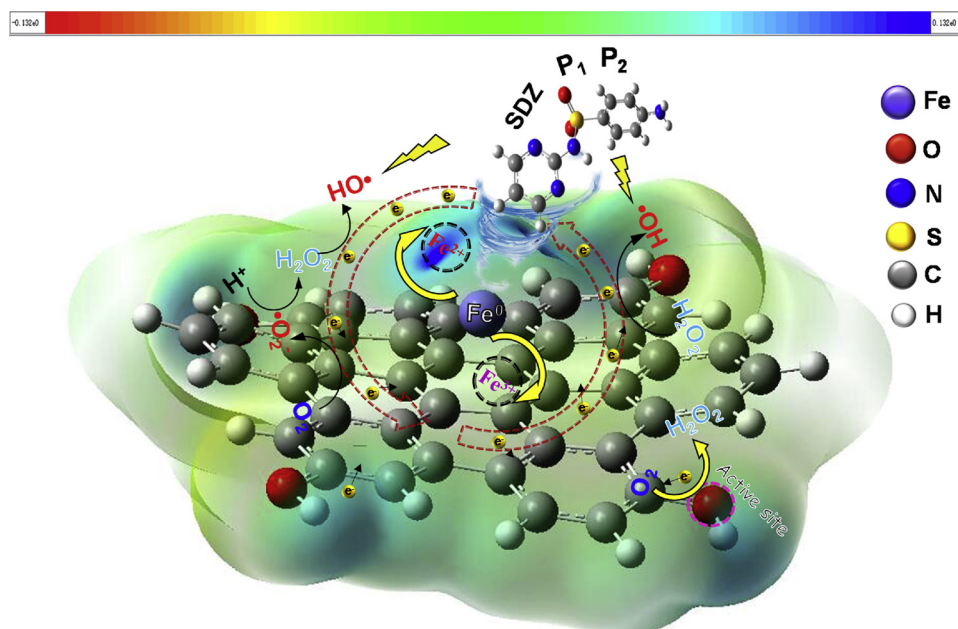


Fig. 15. The proposed reaction mechanism for the removal of sulfadiazine based on the ESP pattern of 3D-GN@nZVI.

Acknowledgements

This work was supported by the National Natural Science Foundation of China (Grant No. 51708238). The authors would like to thank Yankai Li and Yunyun Zou from the shiyanjia lab for ORR and XPS analysis (www.Shiyanjia.com).

References

- N.M. Zhu, Y.S. Xu, L.C. Dai, Y. fei Zhang, G.Q. Hu, Application of sequential extraction analysis to Pb(II) recovery by zerovalent iron-based particles, *J. Hazard. Mater.* 351 (2018) 138–146, <https://doi.org/10.1016/j.jhazmat.2018.03.005>.
- Y.D. Zou, X.X. Wang, A. Khan, P.Y. Wang, Y.H. Liu, A. Alsaedi, T. Hayat, X.K. Wang, Environmental remediation and application of nanoscale zero-valent iron and its composites for the removal of heavy metal ions: a review, *Environ. Sci. Technol.* 50 (2016) 7290–7304, <https://doi.org/10.1021/acs.est.6b01897>.
- R.A. Crane, D.J. Sapsford, Towards “Precision Mining” of wastewater: selective recovery of Cu from acid mine drainage onto diatomite supported nanoscale zero-valent iron particles, *Chemosphere* 202 (2018) 339–348, <https://doi.org/10.1016/j.chemosphere.2018.03.042>.
- H.Y. Shu, M.C. Chang, C.C. Chen, P.E. Chen, Using resin supported nano zero-valent iron particles for decoloration of Acid Blue 113 azo dye solution, *J. Hazard. Mater.* 184 (2010) 499–505, <https://doi.org/10.1016/j.jhazmat.2010.08.064>.
- H.Y. Shu, M.C. Chang, H.H. Yu, W.H. Chen, Reduction of an azo dye Acid Black 24 solution using synthesized nanoscale zerovalent iron particles, *J. Colloid Interface Sci.* 314 (2007) 89–97, <https://doi.org/10.1016/j.jcis.2007.04.071>.
- T. Raychoudhury, T. Scheytt, Potential of zerovalent iron nanoparticles for remediation of environmental organic contaminants in water: a review, *Water Sci. Technol.* 68 (2013) 1425–1439, <https://doi.org/10.2166/wst.2013.358>.
- H.Y. Kim, I.K. Kim, J.H. Shim, Y.C. Kim, T.H. Han, K.C. Chung, P.I. Kim, B.T. Oh, I.S. Kim, Removal of alachlor and pretilachlor by laboratory-synthesized zerovalent iron in pesticide formulation solution, *Bull. Environ. Contam. Toxicol.* 77 (2006) 826–833, <https://doi.org/10.1007/s00128-006-1218-1>.
- T. Satapanajaru, P. Anurakpongsatorn, P. Pengthamkeerati, H. Boparai, Remediation of atrazine-contaminated soil and water by nano zerovalent iron, *Water Air Soil Pollut.* 192 (2008) 349–359, <https://doi.org/10.1007/s11270-008-9661-8>.
- J.H. Chen, X.Q. Qiu, Z.Q. Fang, M. Yang, T. Pokeung, F. Gu, W. Cheng, B.Y. Lan, Removal mechanism of antibiotic metronidazole from aquatic solutions by using nanoscale zero-valent iron particles, *Chem. Eng. J.* 181–182 (2012) 113–119, <https://doi.org/10.1016/j.cej.2011.11.037>.
- X. Liu, Z. Cao, Z.L. Yuan, J. Zhang, X.P. Guo, Y. Yang, F. He, Y.P. Zhao, J. Xu, Insight into the kinetics and mechanism of removal of aqueous chlorinated nitroaromatic antibiotic chloramphenicol by nanoscale zero-valent iron, *Chem. Eng. J.* 334 (2018) 508–518, <https://doi.org/10.1016/j.cej.2017.10.060>.
- C.L. Lee, C.J.G. Jou, Reduced degradation of chlorobenzene in cosolvent solution using nanoscale zerovalent iron with microwave irradiation, *Environ. Eng. Sci.* 28 (2011) 191–195, <https://doi.org/10.1089/ees.2010.0152>.
- M. Velimirovic, M. Auffan, L. Carniato, V. Micić Batka, D. Schmid, S. Wagner, D. Borschneck, O. Proux, F. von der Kammer, T. Hofmann, Effect of field site hydrogeochemical conditions on the corrosion of milled zerovalent iron particles and their dechlorination efficiency, *Sci. Total Environ.* 618 (2018) 1619–1627, <https://doi.org/10.1016/j.scitotenv.2017.10.002>.
- W. Wang, Y.L. Hua, S.L. Li, W. Le Yan, W.X. Zhang, Removal of Pb(II) and Zn(II) using lime and nanoscale zero-valent iron (nZVI): a comparative study, *Chem. Eng. J.* 304 (2016) 79–88, <https://doi.org/10.1016/j.cej.2016.06.069>.
- G. Vilardi, D. Sebastiani, S. Miliziano, N. Verdone, L. Di Palma, Heterogeneous nZVI-induced Fenton oxidation process to enhance biodegradability of excavation by-products, *Chem. Eng. J.* 335 (2018) 309–320, <https://doi.org/10.1016/j.cej.2017.10.152>.
- Y.G. Kang, H. Yoon, W. Lee, E. ju Kim, Y.S. Chang, Comparative study of peroxide oxidants activated by nZVI: removal of 1,4-dioxane and arsenic(III) in contaminated waters, *Chem. Eng. J.* 334 (2018) 2511–2519, <https://doi.org/10.1016/j.cej.2017.11.076>.
- C. Kim, J.Y. Ahn, T.Y. Kim, W.S. Shin, I. Hwang, Activation of persulfate by nanosized zero-valent iron (nZVI): mechanisms and transformation products of nZVI, *Environ. Sci. Technol.* 52 (2018) 3625–3633, <https://doi.org/10.1021/acs.est.7b05847>.
- J.S. Du, W.Q. Guo, H.Z. Wang, R.L. Yin, H.S. Zheng, X.C. Feng, D. Che, N.Q. Ren, Hydroxyl radical dominated degradation of aquatic sulfamethoxazole by Fe⁰/bi-sulfite/O₂: kinetics, mechanisms, and pathways, *Water Res.* 138 (2018) 323–332, <https://doi.org/10.1016/j.watres.2017.12.046>.
- C. Lee, C.R. Keenan, D.L. Sedlak, Polyoxometalate-enhanced oxidation of organic compounds by nanoparticulate zero-valent iron and ferrous ion in the presence of oxygen, *Environ. Sci. Technol.* 42 (2008) 4921–4926, <https://doi.org/10.1021/es800317j>.
- C.M. Wang, D.R. Baer, J.E. Amonette, M.H. Engelhard, J. Antony, Y. Qiang, Morphology and electronic structure of the oxide shell on the surface of iron nanoparticles, *J. Am. Chem. Soc.* 131 (2009) 8824–8832, <https://doi.org/10.1021/ja900353f>.
- L. Ling, X.Y. Huang, M.R. Li, W.X. Zhang, Mapping the reactions in a single zero-valent iron nanoparticle, *Environ. Sci. Technol.* 51 (2017) 14293–14300, <https://doi.org/10.1021/acs.est.7b02233>.
- Y.C. Fu, L. Peng, Q.R. Zeng, Y. Yang, H.J. Song, J.H. Shao, S.Y. Liu, J.D. Gu, High efficient removal of tetracycline from solution by degradation and flocculation with nanoscale zerovalent iron, *Chem. Eng. J.* 270 (2015) 631–640, <https://doi.org/10.1016/j.cej.2015.02.070>.
- X.Q. Peng, X.C. Liu, Y.Y. Zhou, B. Peng, L. Tang, L. Luo, B.S. Yao, Y.C. Deng, J. Tang, G.M. Zeng, New insights into the activity of a biochar supported nanoscale zerovalent iron composite and nanoscale zero valent iron under anaerobic or aerobic conditions, *RSC Adv.* 7 (2017) 8755–8761, <https://doi.org/10.1039/c6ra27256h>.
- J.T. Nurmi, P.G. Tratnyek, V. Sarathy, D.R. Baer, J.E. Amonette, K. Pecher, C. Wang, J.C. Linehan, D.W. Matson, R.L. Penn, M.D. Driessen, Characterization and properties of metallic iron nanoparticles: spectroscopy, electrochemistry, and kinetics, *Environ. Sci. Technol.* 39 (2005) 1221–1230, <https://doi.org/10.1021/es049190u>.
- Y.Y. Ma, X.F. Lv, Q.L. Yang, Y.Y. Wang, X. Chen, Reduction of carbon tetrachloride by nanoscale palladized zero-valent iron@ graphene composites: kinetics, activation energy, effects of reaction conditions and degradation mechanism, *Appl. Catal. A Gen.* 542 (2017) 252–261, <https://doi.org/10.1016/j.apcata.2017.05.028>.
- T.H. Zheng, J.J. Zhan, J.B. He, C. Day, Y.F. Lu, G.L. Mcpherson, G. Piringir, V.T. John, Reactivity characteristics of nanoscale zerovalent iron-silica composites for trichloroethylene remediation, *Environ. Sci. Technol.* 42 (2008) 4494–4499,

- <https://doi.org/10.1021/es702214x>.
- [26] S. Chen, J. Bedia, H. Li, L.Y. Ren, F. Naluswata, C. Belver, Nanoscale zero-valent iron@mesoporous hydrated silica core-shell particles with enhanced dispersibility, transportability and degradation of chlorinated aliphatic hydrocarbons, *Chem. Eng. J.* 343 (2018) 619–628, <https://doi.org/10.1016/j.cej.2018.03.011>.
 - [27] D.J. Zhang, Y. Li, S.Q. Tong, X.B. Jiang, L.J. Wang, X.Y. Sun, J.S. Li, X.D. Liu, J.Y. Shen, Biochar supported sulfide-modified nanoscale zero-valent iron for the reduction of nitrobenzene, *RSC Adv.* 8 (2018) 22161–22168, <https://doi.org/10.1039/c8ra04314k>.
 - [28] Z.M. Jiang, L. Lv, W.M. Zhang, Q. Du, B.C. Pan, L. Yang, Q.X. Zhang, Nitrate reduction using nanosized zero-valent iron supported by polystyrene resins: role of surface functional groups, *Water Res.* 45 (2011) 2191–2198, <https://doi.org/10.1016/j.watres.2011.01.005>.
 - [29] H.R. Dong, F. Zhao, Q. He, Y.K. Xie, Y.L. Zeng, L.H. Zhang, L. Tang, G.M. Zeng, Physicochemical transformation of carboxymethyl cellulose-coated zero-valent iron nanoparticles (nZVI) in simulated groundwater under anaerobic conditions, *Sep. Purif. Technol.* 175 (2017) 376–383, <https://doi.org/10.1016/j.seppur.2016.11.053>.
 - [30] H.R. Dong, F. Zhao, G.M. Zeng, L. Tang, C.Z. Fan, L.H. Zhang, Y.L. Zeng, Q. He, Y.K. Xie, Y. Wu, Aging study on carboxymethyl cellulose-coated zero-valent iron nanoparticles in water: chemical transformation and structural evolution, *J. Hazard. Mater.* 312 (2016) 234–242, <https://doi.org/10.1016/j.jhazmat.2016.03.069>.
 - [31] X.Y. Wang, P. Wang, J. Ma, H.L. Liu, P. Ning, Synthesis, characterization, and reactivity of cellulose modified nano zero-valent iron for dye discoloration, *Appl. Surf. Sci.* 345 (2015) 57–66, <https://doi.org/10.1016/j.apsusc.2015.03.131>.
 - [32] N. Ezzatahmedi, G.A. Ayoko, G.J. Millar, R. Speight, C. Yan, J. Li, S. Li, J. Zhu, Y. Xi, Clay-supported nanoscale zero-valent iron composite materials for the remediation of contaminated aqueous solutions: a review, *Chem. Eng. J.* 312 (2017) 336–350, <https://doi.org/10.1016/j.cej.2016.11.154>.
 - [33] T. Ando, The electronic properties of graphene and carbon nanotubes, *NPG Asia Mater.* 1 (2009) 17–21, <https://doi.org/10.1038/10.1038/asiamat.2009.1>.
 - [34] A. Chutia, F. Cimpoesu, H. Tsuboi, A. Miyamoto, Influence of surface chemistry on the electronic properties of graphene nanoflakes, *Chem. Phys. Lett.* 503 (2011) 91–96, <https://doi.org/10.1016/j.cplett.2010.12.057>.
 - [35] Y. Zhou, Q.L. Bao, L.A.L. Tang, Y.L. Zhong, K.P. Loh, Hydrothermal dehydration for the “green” reduction of exfoliated graphene oxide to graphene and demonstration of tunable optical limiting properties, *Chem. Mater.* 21 (2009) 2950–2956, <https://doi.org/10.1021/cm9006603>.
 - [36] Q.H. Wu, C. Feng, C. Wang, Z. Wang, A facile one-pot solvothermal method to produce superparamagnetic graphene-Fe₃O₄ nanocomposite and its application in the removal of dye from aqueous solution, *Colloids Surf. B Biointerfaces* 101 (2013) 210–214, <https://doi.org/10.1016/j.colsurfb.2012.05.036>.
 - [37] A.A. Isari, A. Payan, M. Fattahi, S. Jorfi, B. Kakavandi, Photocatalytic degradation of rhodamine B and real textile wastewater using Fe-doped TiO₂ anchored on reduced graphene oxide (Fe-TiO₂/rGO): characterization and feasibility, mechanism and pathway studies, *Appl. Surf. Sci.* 462 (2018) 549–564, <https://doi.org/10.1016/j.apsusc.2018.08.133>.
 - [38] U. Farooq, M. Danish, S. Lu, M. Naqvi, X. Gu, X. Fu, X. Zhang, M. Nasir, Synthesis of nZVI/reduced graphene oxide: an efficient catalyst for degradation of 1,1,1-trichloroethane (TCA) in percarbonate system, *Res. Chem. Intermed.* 43 (2017) 3219–3236, <https://doi.org/10.1007/s11164-016-2821-3>.
 - [39] J.W. Shie, Y.L. Li, R. Villegas Salvatierra, T. Wang, P. Dong, Y. Ji, S.K. Lee, C.H. Zhang, J.B. Zhang, R.H. Smith, P.M. Ajayan, J. Lou, N. Zhao, J.M. Tour, Three-dimensional printed graphene foams, *ACS Nano* 11 (2017) 6860–6867, <https://doi.org/10.1021/acsnano.7b01987>.
 - [40] W.J. Liu, J. Wei, X.W. Sun, H.Y. Yu, A study on graphene-metal contact, *Crystals* 3 (2013) 257–274, <https://doi.org/10.3390/cryst3010257>.
 - [41] L.J. Xu, Y.J. Yang, W.Y. Li, Y.J. Tao, Z.G. Sui, S. Song, J. Yang, Three-dimensional macroporous graphene-wrapped zero-valent copper nanoparticles as efficient micro-electrolysis-promoted Fenton-like catalysts for metronidazole removal, *Sci. Total Environ.* 658 (2019) 219–233, <https://doi.org/10.1016/j.scitotenv.2018.12.040>.
 - [42] A. Shimizu, M. Tokumura, K. Nakajima, Y. Kawase, Phenol removal using zero-valent iron powder in the presence of dissolved oxygen: roles of decomposition by the Fenton reaction and adsorption/precipitation, *J. Hazard. Mater.* 201–202 (2012) 60–67, <https://doi.org/10.1016/j.jhazmat.2011.11.009>.
 - [43] S. Guo, G.K. Zhang, Green synthesis of a bifunctional Fe-montmorillonite composite during the Fenton degradation process and its enhanced adsorption and heterogeneous photo-Fenton catalytic properties, *RSC Adv.* 6 (2016) 2537–2545, <https://doi.org/10.1039/c5ra25096j>.
 - [44] W. Liu, J. Qian, K. Wang, H. Xu, D. Jiang, Q. Liu, X.W. Yang, H.M. Li, Magnetically separable Fe₃O₄ nanoparticles-decorated reduced graphene oxide nanocomposite for catalytic wet hydrogen peroxide oxidation, *J. Inorg. Organomet. Polym. Mater.* 23 (2013) 907–916, <https://doi.org/10.1007/s10904-013-9863-4>.
 - [45] T. Zeng, S. Li, J.N. Hua, Z.Q. He, X. Le Zhang, H.R. Feng, S. Song, Synergistically enhancing Fenton-like degradation of organics by in situ transformation from Fe₃O₄ microspheres to mesoporous Fe, N-dual doped carbon, *Sci. Total Environ.* 645 (2018) 550–559, <https://doi.org/10.1016/j.scitotenv.2018.07.162>.
 - [46] J.R. Kim, S.G. Huling, E. Kan, Effects of temperature on adsorption and oxidative degradation of bisphenol A in an acid-treated iron-amended granular activated carbon, *Chem. Eng. J.* 262 (2015) 1260–1267, <https://doi.org/10.1016/j.cej.2014.10.065>.
 - [47] Z. Wan, J.L. Wang, Degradation of sulfamethazine using Fe₃O₄-Mn₃O₄/reduced graphene oxide hybrid as Fenton-like catalyst, *J. Hazard. Mater.* 324 (2017) 653–664, <https://doi.org/10.1016/j.jhazmat.2016.11.039>.
 - [48] W.S. Hummers Jr, R.E. Offeman, Preparation of graphitic oxide, *J. Am. Chem. Soc.* 80 (1958) 1339 <https://pubs.acs.org/sharingguidelines>.
 - [49] K. Raghavachari, Perspective on “Density functional thermochemistry. III. The role of exact exchange,” *Theor. Chem. Acc.* 103 (2000) 361–363, <https://doi.org/10.1007/s002149900065>.
 - [50] D. Andrae, U. Häußermann, M. Dolg, H. Stoll, H. Preuß, Energy-adjusted ab initio pseudopotentials for the second and third row transition elements: molecular test for M₂ (M = Ag, Au) and MH (M = Ru, Os), *Theor. Chim. Acta* 78 (1991) 247–266, <https://doi.org/10.1007/BF01112848>.
 - [51] S. Grimme, J. Antony, S. Ehrlich, H. Krieg, A consistent and accurate ab initio parametrization of density functional dispersion correction (DFT-D) for the 94 elements H-Pu, *J. Chem. Phys.* 132 (2010) 1–18, <https://doi.org/10.1063/1.3382344>.
 - [52] A.V. Marenich, C.J. Cramer, D.G. Truhlar, Universal solvation model based on solute electron density and on a continuum model of the solvent defined by the bulk dielectric constant and atomic surface tensions, *J. Phys. Chem. B* 113 (2009) 6378–6396, <https://doi.org/10.1021/jp810292n>.
 - [53] S. Muthu, R. Rama, K. Sasaki, C. Min, A mechanistic investigation of highly stable nano ZnO decorated nitrogen-rich azacytosine tethered graphene oxide-based dendrimer for the removal of arsenite from water, *Chem. Eng. J.* 370 (2019) 1474–1484, <https://doi.org/10.1016/j.cej.2019.03.277>.
 - [54] S. Sadhukhan, T. Kumar, I. Roy, D. Rana, A. Bhattacharyya, R. Saha, S. Chattopadhyay, S. Khatua, Green synthesis of cadmium oxide decorated reduced graphene oxide nanocomposites and its electrical and antibacterial properties, *Mater. Sci. Eng. C* 99 (2019) 696–709, <https://doi.org/10.1016/j.msec.2019.01.128>.
 - [55] M. Kruk, M. Jaroniec, Gas adsorption characterization of ordered organic-inorganic nanocomposite materials, *Chem. Mater.* 13 (2001) 3169–3183, <https://doi.org/10.1021/cm0101069>.
 - [56] Z.H. Ni, Y.Y. Wang, T. Yu, Z.X. Shen, Raman spectroscopy and imaging of graphene, *Nano Res.* 1 (2008) 273–291, <https://doi.org/10.1007/s12274-008-8036-1>.
 - [57] X.Y. Wang, A.Q. Wang, M.Y. Lu, J. Ma, Synthesis of magnetically recoverable Fe⁰/graphene-TiO₂ nanowires composite for both reduction and photocatalytic oxidation of metronidazole, *Chem. Eng. J.* 337 (2018) 372–384, <https://doi.org/10.1016/j.cej.2017.12.090>.
 - [58] L. Mahmoudian, A. Rashidi, H. Dehghani, R. Rahighi, Single-step scalable synthesis of three-dimensional highly porous graphene with favorable methane adsorption, *Chem. Eng. J.* 304 (2016) 784–792, <https://doi.org/10.1016/j.cej.2016.07.015>.
 - [59] G.F. Yu, L. Lyu, F.G. Zhang, D.B. Yan, W.R. Cao, C. Hu, Theoretical and experimental evidence for rGO-4-PP NC as a metal-free Fenton-like catalyst by tuning the electron distribution, *RSC Adv.* 8 (2018) 3312–3320, <https://doi.org/10.1039/c7ra12573a>.
 - [60] Z. Hasanade, H. Raissi, Assessment of the chitosan-functionalized graphene oxide as a carrier for loading thioguanine, an antitumor drug and effect of urea on adsorption process: combination of DFT computational and molecular dynamics simulation studies, *J. Biomol. Struct. Dyn.* 37 (2018) 2487–2497, <https://doi.org/10.1080/07391102.2018.1496140>.
 - [61] S. Chu, Y. Wang, Y. Guo, J.Y. Feng, C.C. Wang, W.J. Luo, X.X. Fan, Z.G. Zou, Band structure engineering of carbon nitride: in search of a polymer photocatalyst with high photooxidation property, *ACS Catal.* 3 (2013) 912–919, <https://doi.org/10.1021/cs4000624>.
 - [62] L.J. Xu, J.L. Wang, A heterogeneous Fenton-like system with nanoparticulate zero-valent iron for removal of 4-chloro-3-methyl phenol, *J. Hazard. Mater.* 186 (2011) 256–264, <https://doi.org/10.1016/j.jhazmat.2010.10.116>.
 - [63] Y. Liu, Q. Fan, J.L. Wang, Zn-Fe-CNTs catalytic in situ generation of H₂O₂ for Fenton-like degradation of sulfamethoxazole, *J. Hazard. Mater.* 342 (2018) 166–176, <https://doi.org/10.1016/j.jhazmat.2017.08.016>.
 - [64] J.T. Tang, J.L. Wang, Metal organic framework with coordinatively unsaturated sites as efficient Fenton-like catalyst for enhanced degradation of sulfamethazine, *Environ. Sci. Technol.* 52 (2018) 5367–5377, <https://doi.org/10.1021/acs.est.8b00092>.
 - [65] J.F. Bai, Y. Liu, X.H. Yin, H.T. Duan, J.H. Ma, Efficient removal of nitrobenzene by Fenton-like process with Co-Fe layered double hydroxide, *Appl. Surf. Sci.* 416 (2017) 45–50, <https://doi.org/10.1016/j.apsusc.2017.04.117>.
 - [66] Z.Q. Fang, J.H. Chen, X.H. Qiu, X.Q. Qiu, W. Cheng, L.C. Zhu, Effective removal of antibiotic metronidazole from water by nanoscale zero-valent iron particles, *Desalination* 268 (2011) 60–67, <https://doi.org/10.1016/j.desal.2010.09.051>.
 - [67] C.C. Lin, S.T. Hsu, Performance of nZVI/H₂O₂ process in degrading polyvinyl alcohol in aqueous solutions, *Sep. Purif. Technol.* 203 (2018) 111–116, <https://doi.org/10.1016/j.seppur.2018.03.041>.
 - [68] J.C. Yan, L.B. Qian, W.G. Gao, Y. Chen, D. Ouyang, M.F. Chen, Enhanced Fenton-like degradation of trichloroethylene by hydrogen peroxide activated with nanoscale zero valent iron loaded on Biochar, *Sci. Rep.* 7 (2017) 1–9, <https://doi.org/10.1038/srep43051>.
 - [69] Y.M. Su, D. Jassby, S.K. Song, X.F. Zhou, H.Y. Zhao, J. Filip, E. Petala, Y.L. Zhang, Enhanced oxidative and adsorptive removal of diclofenac in heterogeneous Fenton-like reaction with sulfide modified nanoscale zerovalent iron, *Environ. Sci. Technol.* 52 (2018) 6466–6475, <https://doi.org/10.1021/acs.est.8b00231>.
 - [70] L.J. Xu, J.L. Wang, Degradation of chlorophenols using a novel Fe⁰/CeO₂ composite, *Appl. Catal. B Environ.* 142–143 (2013) 396–405, <https://doi.org/10.1016/j.apcatb.2013.05.065>.
 - [71] L.J. Xu, J.L. Wang, Magnetic nanoscale Fe₃O₄/CeO₂ composite as an efficient fenton-like heterogeneous catalyst for degradation of 4-chlorophenol, *Environ. Sci. Technol.* 46 (2012) 10145–10153, <https://doi.org/10.1021/es300303f>.
 - [72] A. Khataee, S. Sajjadi, S. Rahim, A. Hasanadeh, A comparative study on electro-generation of hydrogen peroxide through oxygen reduction over various plasma-

- treated graphite electrodes, *Electrochim. Acta* 244 (2017) 38–46, <https://doi.org/10.1016/j.electacta.2017.05.069>.
- [73] H. Wang, W. Wang, M. Gui, M. Asif, Z. Wang, Y. Yu, J. Xiao, Uniform Fe₃O₄/nitrogen-doped mesoporous carbon spheres derived from ferric citrate-bonded melamine resin as an efficient synergistic catalyst for oxygen reduction, *ACS Appl. Mater. Interfaces* 9 (2017) 335–344, <https://doi.org/10.1021/acsami.6b11608>.
- [74] D. Wang, H. Hou, J. Hu, J. Xu, L. Huang, S. Hu, S. Liang, K. Xiao, B. Liu, J. Yang, A bio-electro-Fenton system with a facile anti-biofouling air cathode for efficient degradation of land fill leachate, *Chemosphere* 215 (2019) 173–181, <https://doi.org/10.1016/j.chemosphere.2018.10.018>.
- [75] T. Zhou, X.L. Zou, J. Mao, X.H. Wu, Decomposition of sulfadiazine in a sonochemical Fe⁰-catalyzed persulfate system: parameters optimizing and interferences of wastewater matrix, *Appl. Catal. B Environ.* 185 (2016) 31–41, <https://doi.org/10.1016/j.apcatb.2015.12.004>.
- [76] J.F. Yang, S.B. Zhou, A.G. Xiao, W.J. Li, G.G. Ying, Chemical oxidation of sulfadiazine by the Fenton process: kinetics, pathways, toxicity evaluation, *J. Environ. Sci. Heal. Part B Pestic. Food Contam. Agric. Wastes* 49 (2014) 909–916, <https://doi.org/10.1080/03601234.2014.951572>.
- [77] J. Gao, C. Hedman, C. Liu, T. Guo, J.A. Pedersen, Transformation of sulfamethazine by manganese oxide in aqueous solution, *Environ. Sci. Technol.* 46 (2012) 2642–2651, <https://doi.org/10.1021/es202492h>.
- [78] J.F. Yang, L.M. Yang, G.G. Ying, C. Bin Liu, L.Y. Zheng, S.L. Luo, Reaction of antibiotic sulfadiazine with manganese dioxide in aqueous phase: kinetics, pathways and toxicity assessment, *J. Environ. Sci. Heal. Part A Toxic/Hazardous Subst. Environ. Eng.* 52 (2017) 135–143, <https://doi.org/10.1080/10934529.2016.1237138>.
- [79] W. Le Yan, A.A. Herzing, X.Q. Li, C.J. Kiely, W.X. Zhang, Structural evolution of Pd-doped nanoscale zero-valent iron (nZVI) in aqueous media and implications for particle aging and reactivity, *Environ. Sci. Technol.* 44 (2010) 4288–4294, <https://doi.org/10.1021/es100051q>.
- [80] M. Dickinson, T.B. Scott, The application of zero-valent iron nanoparticles for the remediation of a uranium-contaminated waste effluent, *J. Hazard. Mater.* 178 (2010) 171–179, <https://doi.org/10.1016/j.jhazmat.2010.01.060>.
- [81] J.S. Cao, X.Q. Li, J. Tavakoli, W.X. Zhang, Temperature programmed reduction for measurement of oxygen content in nanoscale zero-valent iron, *Environ. Sci. Technol.* 42 (2008) 3780–3785, <https://doi.org/10.1021/es7027845>.
- [82] J. Yu, H. Wang, Q. Ji, Investigating adsorption mechanism and surface complex formation modeling for aqueous sulfadiazine bonding on Fe/Mn binary oxides, *Environ. Sci. Pollut. Res.* (2019) 1–11, <https://doi.org/10.1007/s11356-019-05611-2>.
- [83] C.Q. Zhao, P.D. Hong, Y.J. Li, X.M. Song, Y.G. Wang, Y.S. Yang, Mechanism of adsorption of tetracycline–Cu multi-pollutants by graphene oxide (GO) and reduced graphene oxide (rGO), *J. Chem. Technol. Biotechnol.* 94 (2019) 1176–1186, <https://doi.org/10.1002/jctb.5864>.
- [84] X. Peng, X. Liu, Y. Zhou, B. Peng, L. Tang, L. Luo, B. Yao, Y. Deng, J. Tang, G. Zeng, New insights into the activity of a biochar supported nanoscale zerovalent iron composite and nanoscale zero valent iron under anaerobic or aerobic conditions, *RSC Adv.* 7 (2017) 8755–8761, <https://doi.org/10.1039/C6RA27256H>.
- [85] D.L. Sedlak, Factors affecting the yield of oxidants from the reaction of nanoparticulate zero-valent iron and oxygen, *Environ. Sci. Technol.* 42 (2008) 1262–1267, <https://doi.org/10.1021/es7025664>.